HHS Public Access

Author manuscript

Hum Brain Mapp. Author manuscript; available in PMC 2015 August 01.

Published in final edited form as:

Hum Brain Mapp. 2014 August ; 35(8): 3701–3725. doi:10.1002/hbm.22431.

Shape Abnormalities of Subcortical and Ventricular Structures in Mild Cognitive Impairment and Alzheimer's Disease: Detecting, Quantifying, and Predicting

Xiaoying Tang[1,2], **Dominic Holland**[3], **Anders M. Dale**[3,4], **Laurent Younes**[1,5,6], and **Michael I. Miller**[1,5,7] **for the Alzheimer's Disease Neuroimaging Initiative**[*]

[1]Center for Imaging Science, Johns Hopkins University, Baltimore, MD, USA

[2]Department of Electrical and Computer Engineering, Johns Hopkins University, Baltimore, MD, USA

[3]Department of Neurosciences, University of California, San Diego, La Jolla, CD, USA

[4]Department of Radiology, University of California, San Diego, La Jolla, CA, USA

[5]Institute for Computational Medicine, Johns Hopkins University, Baltimore, MD, USA

[6]Department of Applied Mathematics and Statistics, Johns Hopkins University, Baltimore, USA

[7]Department of Biomedical Engineering, Johns Hopkins University, Baltimore, MD, USA

Abstract

This article assesses the feasibility of using shape information to detect and quantify the subcortical and ventricular structural changes in mild cognitive impairment (MCI) and Alzheimer's disease (AD) patients. We first demonstrate structural shape abnormalities in MCI and AD as compared with healthy controls (HC). Exploring the development to AD, we then divide the MCI participants into two subgroups based on longitudinal clinical information: (1) MCI patients who remained stable; (2) MCI patients who converted to AD over time. We focus on seven structures (amygdala, hippocampus, thalamus, caudate, putamen, globus pallidus, and lateral ventricles) in 754 MR scans (210 HC, 369 MCI of which 151 converted to AD over time, and 175 AD). The hippocampus and amygdala were further subsegmented based on high field 0.8 mm isotropic 7.0T scans for finer exploration. For MCI and AD, prominent ventricular expansions were detected and we found that these patients had strongest hippocampal atrophy occurring at CA1 and strongest amygdala atrophy at the basolateral complex. Mild atrophy in basal ganglia structures was also detected in MCI and AD. Stronger atrophy in the amygdala and hippocampus, and greater expansion in ventricles was observed in MCI converters, relative to those MCI who remained stable. Furthermore, we performed principal component analysis on a linear shape space of each structure. A subsequent linear discriminant analysis on the principal component values of

[*]Correspondence to: Michael I. Miller, 301 Clark Hall, 3400 N. Charles Street, Baltimore, 21218, MD, USA. mim@cis.jhu.edu.

[*]Data used in preparation of this article were obtained from the Alzheimer's Disease Neuroimaging Initiative (ADNI) database (adni.loni.ucla.edu). As such, the investigators within the ADNI contributed to the design and implementation of ADNI and/or provided data but did not participate in analysis or writing of this report. A complete listing of ADNI investigators can be found at: http://adni.loni.ucla.edu/wp-content/uploads/how_to_apply/ADNI_Acknowledgemen_List.pdf

hippocampus, amygdala, and ventricle leads to correct classification of 88% HC subjects and 86% AD subjects.

Keywords

Alzheimer's disease; mild cognitive impairment; subcortical structures; lateral ventricles; high field; subsegmentations; shape abnormality; large deformation diffeomorphic metric mapping

INTRODUCTION

Alzheimer's disease (AD) is a neurodegenerative brain disorder characterized by a progressive dementia that increases in incidence with increasing age [McKhann et al., 1984]. AD has been reported to be of an average prevalence, about 50%, among patients with dementia [Ferri et al., 2005]. Mild cognitive impairment (MCI) is a syndrome regarded as a risk state for dementia [Gauthier et al., 2006] and is associated with an increased risk of progression to probable AD [Morris et al., 2001]. Even though more than half of individuals with MCI deteriorate to dementia within 5 years [Gauthier et al., 2006], considerable heterogeneity exists among MCI patients: some remain stable for a long time, others revert to normal cognitive status, and still others develop dementia other than AD [Larrieu et al., 2002]. The ability to identify an MCI patient's risk of developing AD is crucial for clinical decision-making. Thus, more substantial exploration of subtypes of MCI is needed to facilitate the predictive prognosis of which MCI individuals are likely to deteriorate to AD. Methods of detecting MCI that represents prodromal AD would aid clinical practice by allowing attention to be focused on those with the highest risk of conversion.

Structural neuroimaging measures have been widely used to differentiate healthy controls (HC) from subjects with dementia of Alzheimer type because these measures are sensitive to the degeneration that occurs in MCI and AD [Ramani et al., 2006]. Detecting structural changes in the pre-dementia state would enable early treatment before the development of significant functional impairment or neuronal damage. Volumetric assessment, comparing the volumes of various brain structures across subjects from the three different groups, is the most popular and direct way. Researchers in prior studies have focused primarily on medial temporal regions, demonstrating atrophy of hippocampus and entorhinal cortex in individuals with MCI or AD compared to those measured in controls [Atiya et al., 2003; Bell-McGinty et al., 2002; Dickerson et al., 2001; Frisoni and Caroli, 2007; Jack et al., 1999; Killiany et al., 2002] and ventricle enlargement in both MCI and AD [Chetelat and Baron, 2003; McKhann et al., 1984; Ridha et al., 2008]. Volumes of other subcortical nuclei such as amygdala, putamen, caudate, and thalamus have also been reported to be affected in MCI and AD [Convit et al., 2000; de Jong et al., 2008; Madsen et al., 2010; Visser et al., 1999; Whitehouse et al., 1982]. In addition to the magnitude and pattern of structural changes, increase in the rate of these changes with disease progression has also been widely studied in MCI and AD [Barnes et al., 2009; Henneman et al., 2009; Holland et al., 2011; Jack et al., 2009; McDonald et al., 2009; Sluimer et al., 2009].

One potential limitation of the volume-based analysis is that the change of the volume size of a single structure does not provide detailed information about the specific subregions

showing atrophy or expansion. Evaluating the volume size of a structure makes it difficult to identify the specific regions in the structure that are most affected by the disease. Moreover, for a single structure, it is plausible that a part of it is undergoing atrophy while another part is expanding, which makes the overall volume size unaffected. In this case, simply evaluating whether there is volume change in the structure cannot indicate whether this structure is affected.

To identify the magnitude and the pattern of structural changes in an individual at an early stage or a very mild level AD, new tools that enable the detection of subtle changes in neuroanatomy have been sought. Brain warping techniques such as large deformation diffeomorphic metric mapping (LDDMM) have been reported to characterize region-specific variations in numerous neurodegenerative disease studies in terms of either volume or shape analysis [Csernansky et al., 1998, 2000, 2002, 2005; Qiu et al., 2007, 2008, 2009; Wang et al., 2003, 2006, 2007; Younes et al., in press]. To date, most studies have been focused on specific regions such as hippocampus or lateral ventricle [Apostolova et al., 2006; Csernansky et al., 2005; Ferrarini et al., 2006; Wang et al., 2006]. However, the change of a single structure may not necessarily be specific to MCI or AD [van de Pol et al., 2006]. Incorporating structural information of other subcortical nuclei could aid in identifying the atrophy patterns that are specific to dementia of Alzheimer type. Additionally, an analysis of multiple structures would help in understanding the spreading patterns of the disease in the brain.

So far, the majority of neuroimaging experiments are performed on images acquired from 1.5T or 3.0T magnetic resonance imaging (MRI) scanners. Due to the coarse image resolution of typical structural MRI scans, either the hippocampus or the amygdala is usually regarded as a single entity even though they consist of multiple distinct, interacting subregions. It has been shown that the distinct subregions of hippocampus are affected differently in AD [Fukutani et al., 1995; Small et al., 2000; West et al., 2004]. It would be of great potential value in studying the function of the hippocampus and the amygdala if we could compare HC and MCI as well as AD respectively on each subregion of the two structures. It would also be important in understanding the disease pattern within a single structure. Recent advances in MRI data acquisition technology make it possible to acquire images with higher resolution and signal-to-noise ratio, which allows for the exploration of more fine-scaled features of the hippocampus and the amygdala. However, most existing public datasets do not have images obtained from the high field MRI technology, which is a fundamental bottleneck in studies based on those datasets. LDDMM is capable of transferring the subregion features from a predelineated structural image, acquired from high field scanners, to other structural images with more coarse resolution. In this way, the shape differences among the three groups could be analyzed more finely based on each subregion of the hippocampus and the amygdala.

In this article, we characterize shape abnormalities of seven subcortical and ventricular structures (the lateral ventricular system, memory related amygdala-hippocampal circuit, thalamic and basal ganglia circuits which receive projections from the amygdala and hippocampus) as well as the subregions of the hippocampus and the amygdala in subjects with MCI or AD within the framework of LDDMM [Miller et al., 2002]. One goal of this

study is to quantitatively assess whether the surface (a two-dimensional manifold) contouring a single structure, i.e. the shape, differs as a function of disease severity in prodromal and mild AD and whether it could provide accurate prognostic information in patients with AD. Specifically, the shape differences among the three groups—HC, MCI, and AD are investigated. The MCI populations, at the baseline, are stratified into three subgroups according to the longitudinal clinical information: (1) MCI patients who reverted to normal status; (2) MCI patients who remained stable; (3) MCI patients who deteriorated to AD. The shapes, at the baseline, of these three MCI subtypes are being studied here to determine whether differences exist, and in future studies we will investigate their ability to predict decline. We are particularly interested in characterizing the atrophy patterns in the hippocampus and the amygdala more finely by integration of high-field imaging techniques. Therefore, we refine our study of the atrophy patterns in these two structures to include the CA1, subiculum, and the part consisting of CA2, CA3, and dentate gyrus (three hippocampal subregions), as well as the basolateral, basomedial, centromedial, and lateral nucleus (four subregions of the amygdala) based on two 0.8 mm isotropic 7T MRI scans. Analyzing the shape changes on each subregion of the hippocampus and the amygdala may help understand how the disease spreads within a single structure and identify which part in these structures is most affected by the disease.

In this setting of LDDMM, a deformation is computed as the end point of an energy-minimizing path (a geodesic) through the group of diffeomorphisms. Given a fixed template, the anatomical variability in the targets is encoded by the geodesics from the template to each target. The fundamental “conservation of momentum” property of these geodesics [Miller et al., 2006] allows for representing the entire flow of a geodesic by the initial momentum configuration. Since the geodesic flow at any point is completely determined by the momentum at the origin, this means that, once a template is fixed, the space of initial momenta becomes an appropriate linear vector space [Vaillant et al., 2004] for studying shape. Anatomical differences among different target groups can, therefore, be studied by applying linear statistical analysis such as principal component analysis (PCA) to the initial momentum vectors, which was successfully demonstrated in [Helm et al., 2006; Vaillant et al., 2004; Wang et al., 2007]. PCA followed by linear discriminant analysis (LDA) on the initial momentum may be able to provide a shape-associated biomarker to discriminate between different clinical groups.

We present results from investigations of: (1) anatomical abnormalities in MCI and AD compared with HC in all the seven structures; (2) anatomical abnormalities in MCI and AD specific to each subregion of the hippocampus and the amygdala; (3) shape differences in the three subtypes of MCI in all the seven structures; (4) shape differences in the subregions of the hippocampus and the amygdala among the three MCI subgroups. Finally, we present linear statistics with discrimination on the initial momentum. The discriminating ability of each structure based on its shape information is compared. By combining the shape information of different structures, we identify the optimal LDA classifier we could build, based on this information, to differentiate AD and HC subjects. To estimate the correct classification rate of the optimal LDA classifier, we adopt a two-level leave-one-out cross validation procedure.

METHODS

Alzheimer's Disease Neuroimaging Initiative

Data used in the preparation of this article were obtained from the Alzheimer's Disease Neuroimaging Initiative (ADNI) database (adni.loni.ucla.edu). The ADNI was launched in 2003 by the National Institute on Aging (NIA), the National Institute of Biomedical Imaging and Bioengineering (NIBIB), the Food and Drug Administration (FDA), private pharmaceutical companies and non-profit organizations, as a $60 million, 5-year public–private partnership. The primary goal of ADNI has been to test whether serial magnetic resonance imaging (MRI), positron emission tomography (PET), other biological markers, and clinical and neuropsychological assessment can be combined to measure the progression of mild cognitive impairment (MCI) and early Alzheimer's disease (AD). Determination of sensitive and specific markers of very early AD progression is intended to aid researchers and clinicians to develop new treatments and monitor their effectiveness, as well as lessen the time and cost of clinical trials.

The Principal Investigator of this initiative is Michael W. Weiner, MD, VA Medical Center and University of California, San Francisco. ADNI is the result of efforts of many coinvestigators from a broad range of academic institutions and private corporations, and subjects have been recruited from over 50 sites across the U.S. and Canada. The initial goal of ADNI was to recruit 800 adults, ages 55 to 90, to participate in the research, approximately 200 cognitively normal older individuals to be followed for 3 years, 400 people with MCI to be followed for 3 years and 200 people with early AD to be followed for 2 years. For up-to-date information, see www.adni-info.org.

Participants

In this study, we included data from 210 HC subjects, 369 subjects with MCI, and 175 subjects with AD. Within the MCI group, 369 subjects were further divided into three groups: MCI-HC—those who reverted to normal cognitive status (13 subjects); MCI-MCI—those who remained stable (205 subjects); and MCI-AD—those who converted to AD (151 subjects), according to the clinical information of the population after a follow-up of one year. Since the MCI-HC group is very small, we exclude it from our analysis. We term the MCI-MCI group as MCI-stable. Group clinical and demographic data are presented in Table I. Briefly, subjects are 55 to 92 years old, and are not depressed. The control subjects have Mini-Mental State Examination (MMSE) scores of 25 to 30 and a clinical dementia rating (CDR) of 0. The subjects with MCI have MMSE scores of 23 to 30, a CDR of 0.5, preserved ability to perform daily living activities, and absence of dementia. The subjects with AD have MMSE scores of 20 to 28 and a CDR of 0.5 or 1.0 and meet the criteria for probable AD.

The subject groups did not differ significantly in age (F =2.53, P =0.081). All groups differed on MMSE and clinical dementia rating scale sum of boxes (CDR-SB) as expected based on diagnostic criteria (all $P < 0.001$).

Image Protocol and Volumetric Segmentation

The volume segmentations of all the seven structures were created from raw DICOM MR scans downloaded from the public ADNI website (http://www.loni.u-cla.edu/ADNI/Data/index.shtml). Locally, the raw MR data were automatically corrected for spatial distortion due to gradient nonlinearity [Jovicich et al., 2006] and B1 field inhomogeneity [Sled et al., 1998]. The two T1-weighted images from each subject were rigid-body aligned to each other and then averaged to improve signal-to-noise ratio and resampled to isotropic 1 mm voxels. Volumetric segmentations for the hippocampus, amygdala, caudate, putamen, globus pallidus, thalamus, and lateral ventricle were created using FreeSurfer [Fischl et al., 2002]. Based on the transformation of the full brain mask into atlas space, total cranial vault value was estimated from the atlas scaling factor [Buckner et al., 2004] to control individual differences in head size.

The quality of the automated volumetric segmentations has been reviewed. Failed subjects were excluded from the analysis. Qualitative review was performed, with blinding to the diagnostic status, by one of three technicians who have been trained and supervised by an expert neuroanatomist with more than 10 years of experience, as described in [Holland et al., 2009]. The technicians had a minimum of 4 months of experience reviewing brain MR images prior to their involvement in this project.

Images that suffered degradation due to motion artifacts, technical problems (change in scanner model or change in RF coil during the time-series), or significant clinical abnormalities (e.g., hemispheric infarction) were excluded [Holland et al., 2009, 2012]. As a result, the number of scans was reduced by approximately 15%.

Surface Generation

In preparation for surface-based morphometric analysis, all volumetric segmentations of the seven structures were transformed into triangulated surfaces using a pipeline built on the LDDMM-image algorithm. Qiu et al. [2010] created a template set of the seven structures (left and right), the Computational Functional Anatomy (CFA) subcortical template [Qiu and Miller, 2008], from a separate set of 41 manually labeled volumes. In this CFA subcortical template set, each structure has its three-dimensional binary volume representation as well as a smooth two-dimensional surface contouring the volume. To be specific, the CFA subcortical template consists of 14 binary images $I_{\text{temp}} = \{I_{\text{temp\_struct}_1}, I_{\text{temp\_struct}_2}, \ldots, I_{\text{temp\_struct}_{14}}\}$ and 14 surfaces bounding the corresponding structure images $S_{\text{temp}} = \{S_{\text{temp\_struct}_1}, S_{\text{temp\_struct}_2}, \ldots, S_{\text{temp\_struct}_{14}}\}$. For each subject, the corresponding volume segmentation images of the 14 structures, $I_{\text{sub}_i} = \{I_{\text{sub}_i\text{\_struct}_1}, I_{\text{sub}_i\text{\_struct}_2}, \ldots, I_{\text{sub}_i\text{\_struct}_{14}}\}$, were created by FreeSurfer [Fischl et al., 2002]. A 14-channel LDDMM-image mapping [Ceritoglu et al., 2009] was performed to obtain a diffeomorphic change between the template coordinate system and the subject coordinate system, with each individual channel being the volume image of each structure. To do this, we define a distance function, between the deformed template and the *i*-th subject, as:

$$D\left(I^{\circ}_{\text{temp}}\phi_i^{-1}, I_{\text{sub}_i}\right) = \sum_{j=1}^{14} \left| I^{\circ}_{\text{temp\_ struct}_j}\phi_i^{-1} - I_{\text{sub}_i - \text{struct}_j} \right|^2_{L^2},$$

where the optimizing deformation φ_i is generated as the end point, $\phi_i = \varphi_1^v$, of the flow of smooth time-dependent

vector field, $v_t \in V$, $t \in [0, 1]$ with the ordinary differential equation, $\frac{d\varphi_t^v}{dt} = v_t(\varphi_t^v)$, $t \in [0, 1]$ for V, a reproducing kernel Hilbert space with a smooth kernel and norm $|\cdot|_V$. The optimal diffeomorphism solves the matching problem:

$$E(v) = \int_0^1 |v_t|_V^2 dt + D(I^\circ_{\text{temp}} \phi_i^{-1}, I_{\text{sub}_i}). \quad (1)$$

The deformed template segmentations, corresponding to the i-th subject, are given by:

$$\begin{aligned} \hat{I}_{\text{sub}_i} &= \left\{ \hat{I}_{\text{sub}_i\text{\_ struct}_1}, \hat{I}_{\text{sub}_i\text{\_ struct}_2}, \ldots, \hat{I}_{\text{sub}_i\text{\_ struct}_{14}} \right\} \\ &= \left\{ I^\circ_{\text{temp\_ struct}_1} \phi_i^{-1}, I^\circ_{\text{temp\_ struct}_2} \phi_i^{-1}, \ldots, I^\circ_{\text{temp\_ struct}_{14}} \phi_i^{-1} \right\}. \end{aligned} \quad (2)$$

These can be regarded as the "filtered" or "denoised" approximations of the subject structure segmentations. The surface representations of the subject structures were then created by applying the deformation φ_i to the template surfaces:

$$\begin{aligned} S_{\text{sub}_i} &= \{ S_{\text{sub}_i\text{\_ struct}_1}, S_{\text{sub}_i\text{\_ struct}_2}, \ldots, S_{\text{sub}_i\text{\_ struct}_{14}} \} \\ &= \{ \phi_i \cdot S_{\text{temp\_ struct}_1}, \phi_i \cdot S_{\text{temp\_ struct}_2}, \ldots, \phi_i \cdot S_{\text{temp\_ struct}_{14}} \}. \end{aligned} \quad (3)$$

The surfaces S_{sub_i}, $i = 1, 2, \ldots, 754$ are the ones our statistical analyses were based on in subsequent sections. LDDMM carries the smooth submanifold diffeomorphically, and thus is capable of maintaining the smooth boundary and the correct topology of the template surfaces in the target surfaces [Miller et al., 2006]. This method of surface generation has already been validated in [Qiu and Miller, 2008] in detail. We quantitatively compared the structure volumes after the de-noising procedure with the original FreeSurfer volumes in terms of kappa overlap [Landis and Koch, 1977] and volume difference. As shown in Figure 1, for each structure, an average kappa overlap above 0.85 was obtained. For each structure, the average volume of the segmentations from the de-noising procedure and that of the original FreeSurfer segmentations, as well as their differences are listed in Table II. For a majority of structures, the mean volume discrepancy is within 10%. The discrepancy mostly occurs where the FreeSurfer segmentations are not smooth or have topological errors or thin structures that FreeSurfer is not able to identify in the MR image. Examples of such discrepancies can be found in [Qiu and Miller, 2008].

Template Surface Generation

Our statistical shape analysis within the framework of LDDMM is done on the basis of a template surface. To reduce the difference between the template and the group populations, we generated the template surface from a subset of the populations. For each single structure, every subject surface was first rigidly aligned (rotation and translation) to a common spatial position. The rigid registration algorithm computes an optimal transformation between the vertex sets of two surfaces S_0 and S_1, by minimizing a score combining registration and soft assignment, which is similar to the one considered in [Rangarajan et al., 1997]. In detail, let x_i *(*i = 1, 2, .., *M)* denote the set of vertices on the

template surface, and y_j (j = 1, 2, …, N) the set of vertices on the target surface, the cost function is:

$$E=\lambda(3-tr(R))+\sum_{i=1}^{M}\sum_{j=1}^{N}(w_{ij}+v_{ij})|Rx_i+T-y_j|^2+t(w_{ij}\log w_{ij}+v_{ij}\log v_{ij}) \quad (4)$$

for some $\lambda > 0$, subject to constraints 1, $\sum_{i=1}^{M} w_{ij}=1$, $\sum_{j=1}^{N} v_{ij}=1$, $w_{ij} \geq 0$, $v_{ij} \geq 0$. The term $(3-tr)(R)$) is the regularization term. The matching term and the soft assign term are given by $(w_{ij}+v_{ij})|Rx_i+T-y_j|^2$ and $t(w_{ij}\log w_{ij}+ v_{ij} \log v_{ij})$ respectively. R is the rotation matrix, and $T \in R^3$.

After rigid registration, we computed an averaged template surface, using the algorithm described in [Ma et al., 2010]. Each observed subject surface is modeled as a random deformation of a hidden template plus additive Gaussian noise. Given this model, the template is estimated from the subject surfaces using an approximation of the expectation-maximization (EM) algorithm [Dempster et al., 1977], subject to some topology constraints. It is enacted by ensuring that the hidden template surface is a diffeomorphic deformation of a reference shape, called hypertemplate. Equal proportions of subjects from the three groups were selected for the template averaging, resulting in a total of 270 subjects.

LDDMM-Surface Registration

After obtaining the template surface for each structure, we performed LDDMM-surface mapping [Vaillant and Glaunés, 2005] to compute a diffeomorphic registration between the template and each of the 754 target surfaces for each structure. In the LDDMM setting, the set of anatomical shapes is placed into a metric space. This is modeled by assuming that one shape can be generated from another via group actions of diffeomorphisms, i.e., that compared shapes are topologically equivalent, which is true for the subvolumes that we consider in this article. To compare shapes, we generate time-dependent diffeomorphisms by solving the ordinary differential equation $\varphi_t=v_t(\varphi_t)$, $t \in [0, 1]$ with φ_0 being the identity map and v_t a three-dimensional vector field that will be computed by the algorithm. Given a template surface S_{temp} and a target shape S_{obs} (the observed subject surface), the inexact matching registration algorithm minimizes the functional:

$$E(v)=\inf_{v:\ \dot{\phi}_t=v_t(\phi_t),\ \phi_0=\mathrm{id}} \int_0^1 |v_t|_V^2 dt+D(\phi_1 \cdot S_{temp}, S_{obs}) \quad (5)$$

where $\varphi_1 \cdot S_{temp}$ is the deformed template, resulting from the action of the diffeomorphism at time t =1 on the template surface. The function D is a discrepancy measure between surfaces [Vaillant and Glaunés, 2005]. After minimization, the integral term in the cost function can be interpreted as a squared geodesic distance, in shape space between the template and the deformed template. The norm $|\cdot|_V$ is a Hilbert norm, V being a reproducing kernel Hilbert space of vector fields. To ensure that the solutions are diffeomorphisms, V must be a space of smooth vectors [Dupuis et al., 1998].

The solutions take a special form after discretization. Assume that surfaces are triangulated, and let x^j denote the vertices of the template surface S_{temp}. It has been proved that the solution of Eq. (5) must be of the form

$$v_t(x)=\sum_j k_V(x_t{}^j, x)\alpha_t{}^j \quad (6)$$

where k_V denotes the reproducing kernel of the space V and α is the momentum vector [Camion and Younes, 2001; Joshi and Miller, 2000]. In practice, k_V is selected to be a Gaussian kernel in the sense that $k_V(x,y)=\exp\left(-\frac{|x,y|^2}{2\sigma_V{}^2}\right)$. After reduction, Eq. (5) can be equivalently put in the form:

$$E(\alpha)=\inf_{\alpha_t:\ \dot{\phi}_t=k_V\alpha_t(\phi_t),\ \phi_0=\mathrm{id}} \int_0^1 \alpha_t{}^T K(x_t)\alpha_t dt+D(\phi_1\cdot S_{temp}, S_{obs}) \quad (7)$$

where $K(x_t)$ is the matrix formed with $k_V(x_t^i, x_t^j)$.

Vertex-Based Statistical Analysis

From the LDDMM-surface mapping, we calculate a scalar field on the template surface according to: J=log (det ($D\varphi_t$)), where $D\varphi_t$ is the Jacobian matrix of φ_t. This scalar field measures the expansion or atrophy at each vertex of the subject relative to the template in the logarithmic scale: i.e. positive values correspond to surface expansion of the subject's structure relative to the template at a particular location, while negative values denote surface atrophy of the subject's structure relative to the template. We shall call this scalar field as a "deformation marker" $J_k(s)$ which is indexed at each vertex k of the template surface for each subject s. Similar morphometric statistics have been used in [Ashburner and Friston, 2000; Chiang et al., 2007; Qiu et al., 2009; Wang et al., 2011; Woods, 2003]. This vertex-based analysis (which therefore restricts to shape boundaries) arises naturally for studying shape changes since, in our case, the subcortical structures at 1 mm scale MRI appear constant in contrast (so that little information is available inside the structures).

In our vertex-based statistical group analysis, we introduce a group variable $Y(s)$ to represent one of the groups in comparison. Let $Y(s)$ be equal to 1 if subject s belongs to that group. The statistical model is given by (at each vertex k):

$$J_k(s)=\beta_{k,0}+\beta_{k,1}\Upsilon(s)+\sum_{\mathrm{cov}}\alpha_{\mathrm{cov}}X_{\mathrm{cov}}(s)+\varepsilon_k(s) \quad (8)$$

where $X_{\mathrm{cov}}(s)$ is the covariate information (confounding factors) included in the analysis. In our study, we covaried for age, sex, and the estimated intracranial volume. We tested for the null hypothesis that $\beta_{k,1}=0$ separately for all vertices k. Statistics were therefore computed at each vertex of the triangulated template surface, and P values were corrected for multiple comparisons. More precisely, for each k, we computed the statistic:

$$F_k = \frac{RSS_0(k)}{RSS(k)} - 1 \quad (9)$$

where RSS_0 is the residual sum of squares under the null hypothesis, and RSS the residual sum of squares under the general hypothesis. We then compute $F^* = \max_k F_k$, the maximum value of the statistics over all vertices of the template surface. The statistical significance of differences between the two groups in comparison is measured based on Fisher's method of randomization. We utilized Monte Carlo simulations to generate 40,000 uniformly distributed random permutations of the group labels, which gives rise to a collection of the F^* statistic coming from each permutation. The *p*-value for the significance of the group labels is then given by the fraction of the times that the values F^* from the permutations are larger than the value obtained from the true groups. The set of vertices on which the null hypothesis is not valid is estimated to be:

$$D = \{k : F_k \geq q^*\} \quad (10)$$

where q^* is the 95% value of the collection of the F^* statistic from the permutation tests [Nichols and Hayasaka, 2003] and F_k is the observed statistic at vertex k (with the true labels). To quantify the group shape variation (compression or expansion), we define the degree of the group shape differences as the negative value of the sum of β coefficients associated to the two groups in comparison. Thus, negative values denote expansion in the latter group for comparison while positive values denote atrophy.

In our study, for each structure, we first performed three statistical comparisons between every two of the three groups—HC, MCI, and AD, and then compared the two subtypes of MCI: MCI-stable and MCI-AD.

PCA-Based Analysis

Miller et al. [2006] proved that the optimal momentum, α_t, solution of Eq. (7) satisfies a conservation property: the initial momentum α_0 encodes the geodesic connecting the template surface to the deformed template surface via

$$\alpha_t{}^i = (D\phi_t(x^i))^{-T} \alpha_0{}^i \quad (11)$$

where $()^{-T}$ denotes matrix inverse and transpose and φ_t the diffeomorphism associated to v_t in Eq. (6). The deformations from the LDDMM-surface mappings are completely encoded by the initial momentum α_0 in the template surface coordinates, which allows for linear techniques to be applied to it.

For each structure, we performed principal component analysis (PCA) on the initial momentum α_0 of all the subjects to construct an orthonormal basis. The feature space constructed via the initial momentum was then linearly projected to the orthogonal directions that carry the greatest shape variance. Age, sex, and the estimated intracranial volume information has been corrected using a linear regression model before performing a

nonparametric statistical test, in which we utilized the first M ($M < 754$) coefficients in the principal component basis (PCs) that account for 95% of the total variance.

Nonparametric permutation tests were performed between every two of the three groups. Take group HC and group AD for example. Let $\hat{Z}^{HC}$ and $\hat{Z}^{AD}$ be the sample means of the first M principal component values for the two groups, and $\hat{\Sigma}$ the pooled sample covariance. To test the null hypothesis H_0: $\hat{Z}^{HC}$ and $\hat{Z}^{AD}$, we computed the Hotelling's T^2 statistic [Anderson, 1958] as:

$$T^2 \doteq \frac{N_{HC} \times N_{AD}}{N_{HC}+N_{AD}}(\hat{Z}^{HC}-\hat{Z}^{AD})^T \hat{\sum}^{-1}(\hat{Z}^{HC}-\hat{Z}^{AD}) \quad (12)$$

where N_{HC} is the total number of HC subjects and N_{AD} is the total number of AD subjects. Similar to the vertex-based analysis, we used Monte Carlo simulations to generate random permutations to correct the P values.

The same statistical tests have also been applied to the structure volumes (replacing the principal component values with the structure volume size) for comparison purposes.

Linear Discriminant Analysis

Via non-parametric statistical tests on each set of PCs, we found that group differences between AD and HC exist in a majority of structures. It is natural to try to discriminate between the two groups based on those PC features showing group differences, and we chose linear discriminant analysis (LDA) to do so. In this framework, for the two-class problem, the discriminating direction is the projection of the differences between the two class means onto the common covariance, yielding $K^{-1}(\mu^{HC} - \mu^{AD}$, where K is the common covariance of the two populations, and μ^{HC}, μ^{AD} are the two class means.

In terms of discriminant analysis, we have several different goals: (1) evaluate the performance of the LDA classifiers, trained on the PCs of each single structure, to determine which structure has the most discriminating shape information; (2) determine whether combining the shape information of multiple structures will strengthen the classification effect; (3) determine whether increasing the number of structures we use would improve the accuracy; (4) determine the best LDA classifier we can build based on the shape information of the seven structures; (5) estimate the true classification rate we would obtain from our classification procedure.

To reduce the dimension of the feature space, we selected only the PCs that show significant group difference between HC and AD. For each PC, we did the same non-parametric statistical test as described in PCA-based analysis (PCA-Based Analysis section) and selected those PCs with a p-value less than 0.05 obtained in the permutation test.

To fulfill our goals (1) to (4), we tested all the possible LDA classifiers we could build from the PCs of the seven structures. Considering each possible combination, we built $2^7-1=127$ different classifiers and compared their classification performance with each other based on leave-one-out cross validation. The procedure is demonstrated in Figure 2, and consists of three steps. The first step is to create all the possible feature spaces by combining the

different sets of PCs. Since we have seven sets of PCs, the result is a total of 127 feature spaces. The next step is to test the classification rate based on the feature information in each combination. In this step, we adopt leave-one-out as the cross validation procedure: leave one subject out and train an LDA classifier based on the feature vectors of all the other remaining subjects, then use this LDA to classify the subject excluded at the beginning. In the end, we select the LDA classifier with the highest average correct classification rate in the previous step as our optimal LDA classifier. To test whether shape information is more discriminating than volume information, we performed the same procedure using only the volume information of the structures and compared.

To estimate the true classification rate we would obtain from our classification procedure, we again use leave-one-out as our cross-validation strategy. The cross-validation process is summarized in Figure 3. We exclude the initial momentum of one subject at the very beginning, and then build a PCA basis, based on the initial momentums of all the other remaining subjects, for every structure. Then, we take two steps to reduce the dimensionality of each feature matrix: (1) we select the first N components that account for a 95% of the total variance; (2) among the N feature vectors we keep in (1), we sift the ones with significant group difference, for which we use Student's t-test. After that, we select the optimal LDA classifier via the procedure described in Figure 2. And in the end, the optimal LDA classifier is used to classify the subject removed at the very beginning. This procedure is done for each subject. To determine which structure, among all the seven, exhibits the most discriminating shape information, we tested the classification rate using each single structure. For example, in examining the classification rate of the LDA classifier built from hippocampus shape information, we did not select the optimal LDA classifier for each subject. Instead, we used the LDA classifier built from the shape feature of hippocampus to classify the subject excluded at the very beginning and then took the average.

Transferring the Subregions of Hippocampus and Amygdala Onto the Template Surfaces

Two ultra-high resolution ($0.8mm \times 0.8mm \times 0.8mm$) T1-weighted images were collected using high-field 7T image acquisition technology. One subject (sub#1) was used for manually segmenting the hippocampus into subregions while the other one (sub#2) was used for the left amygdala subsegmentation. Subject sub#1 is a 30-year-old male. And the subject sub#2 is a 42-year-old male. Both subjects are considered healthy by self-report. The two subjects were scanned using a standard MPRAGE protocol in a Philips Achieva 7.0T scanner (TR =4.3 ms, TE =1.95 ms, flip =7, FOV =220 × 220 × 180). As described in the Appendix, the hippocampus in both hemispheres was manually subdivided into three distinct regions: CA1, subiculum, and the remaining part consisting of CA2, CA3, and dentate gyrus, for which we will denote as CA2+CA3+DG. Triangulated surfaces representing the boundaries of the hippocampus as well as its subregions were generated based on the Marching Cube algorithm. Then, the boundaries of the three subregions were projected onto the mother surface (the surface of the hippocampus) by finding the nearest vertex. We performed LDDMM-surface mapping between the hippocampus surface of the high-resolution image and our template hippocampus to connect the two different coordinate systems, and thereby transfer the three subregions of the 7.0T hippocampus onto our template surface. The left amygdala of the other high resolution MRI image was also

subsegmented into four regions: basolateral, basomedial, centromedial, and lateral nucleus. The four subregions were also similarly transferred to the left amygdala template surface used in our study. The process of transferring the three left hippocampus subregions from the 7.0T high-resolution MRI image onto our template surface is illustrated in Figure 4. The boundaries of the subsegmentations of the hippocampus in both hemispheres and the left amygdala are shown in Figure 5 by projection onto the “mother” surface. Group shape variations were then evaluated based on each single subregion.

RESULTS

Comparisons of HC, MCI, and AD

Results obtained from the vertex-based statistical analyses are summarized in Figures 6 to 11, describing regionally-specific group surface differences between HC and AD, HC and MCI, as well as MCI and AD. The figures highlight vertices on the template surfaces at which significant compression or expansion was detected in the latter group at the significance level of $P = 0.05$. To be specific, Figure 6 to 8 respectively show group shape differences detected in those structures near medial temporal regions—the amygdala and the hippocampus, as well as the lateral ventricle. Figure 9 shows the group differences in the basal ganglia regions as well as the thalamus. Figure 10 shows the relative shape variations of all the seven structures in the left hemisphere while Figure 11 shows shape differences in the right hemisphere.

To explore the shape variations between different groups in the amygdala and the hippocampus more finely, and identify subregions that are most affected by MCI or AD pathology, we evaluated the shape differences on each subregion of the left amygdala and the hippocampus in both hemispheres, the subregions of which were transferred from high-field 7T manual segmentations. Figure 12 demonstrates the group surface deformation differences between HC and AD, HC and MCI, as well as MCI and AD in terms of the four compatible compartments of the left amygdala—basolateral, basomedial, centromedial, and lateral nucleus. Figures 13 and 14 show the group shape differences in the three subregions —CA1, CA2+CA3+DG, and subiculum of the left hippocampus and the right hippocampus.

For the PCA-based analysis, the value, *M*, that indicates the number of the main PCs accounting for 95% of the total variance of the initial momentum feature space (consisting of the initial momentum vector of all subjects) was 21 for left amygdala, 24 for right amygdala, 48 for left hippocampus, 49 for right hippocampus, 44 for left ventricle, 40 for right ventricle, 45 for left caudate, 45 for right caudate, 57 for left putamen, 59 for right putamen, 61 for left thalamus, 60 for right thalamus, 30 for left pallidum, and 29 for right pallidum. The value *M* is related to the variability of the structure in the general population. The fact that this value varies from structure to structure may indicate that some structures are more stable than others, in the sense that the variance of those structures with small *M* is concentrated in a small number of components. In testing the true classification rate as described in Figure 3, there will be different PCA bases for different left-out subjects since we do leave-one-out on PCA. Among all the 385 (210 HC subjects and 175 AD subjects) PCA bases that were computed in that way, the amount numbers of selected PCs was were the same for the left amygdala (21 PCs), right amygdala (23 PCs), left hippocampus (46

PCs), right hippocampus (47 PCs), left thalamus (58 PCs), right thalamus (57 PCs), left putamen (55 PCs), right putamen (56PCs), left pallidum (29), right pallidum (28), and left caudate (42 PCs). For the left ventricle, 368 out of 385 PCA bases had 39 vectors (the mean value being 39.0442), while for the right ventricle, 384 out of 385 had 39 vectors (the mean value being 39.0078). Finally, for the right caudate, 303 out of 385 runs selected 43 PC's, with mean value equal to 42.7870. Results obtained from the PCA-based analyses were in strong agreement with those found in the vertex-based analyses. In Figure 15, we plot the empirical distributions of the left amygdala and the left hippocampus from randomized Hotelling's T^2 tests with 40,000 group permutations, between HC and MCI, HC and AD, as well as MCI and AD. The *p*-values were calculated from the random permutation tests, after correcting for age, sex, and the estimated intracranial volume. All the three comparisons show group differences in both the left hippocampus and the left amygdala, as revealed by the *p*-values. The upper bounds of the confidence intervals for all the *p*-values obtained based on PCs and the structure volumes are listed in Table III.

In terms of discriminating between the two groups HC and AD, we found that the shape PC information associated with each individual structure is uniformly significantly more discriminating than the volume information of that structure—i.e. using shape PCs yields better classification accuracy than volume for every single structure. Generally, based on the shape information, the classification errors were reduced by more than 10% for each single structure. The two sets of classification results are listed in Table IV. In addition, Table IV demonstrates that, among all the seven structures, hippocampus exhibits the highest discriminating ability.

Comparing the mean classification rates of all the LDA classifiers obtained from different combinations of sets of PCs, we found that, based on the initial momentum of all the subjects, the optimal LDA classifier came from a combination of three structures—the hippocampus, the amygdala, and the lateral ventricle. This is in agreement with our vertex-based analysis findings, as well as those in the nonparametric statistical analysis, where we found that the strongest shape differences occurred at the hippocampus, the amygdala, and the lateral ventricle. In estimating the true classification rate that could be achieved using our classification pipeline, the optimal LDA classifiers may be different across iterations since the process of selecting the optimal LDA classifier is embedded in the leave-one-out process. For example, when subject 1 is left out, the optimal LDA classifier comes from a combination of hippocampus and amygdala while for subject 2, the optimal one comes from a combination of hippocampus, amygdala, and ventricle. We therefore calculated the percentage of each structure being included in the optimal classifier. We found that among all optimal LDA classifiers, hippocampus has been selected 88% of the time, amygdala 83% of the time, ventricle 71% of the time, thalamus 45% of the time, caudate 36% of the time, putamen 37% of the time, and pallidum 26% of the time. This, to some degree, confirms our conclusion that if we were to design a single classifier based on the information from all the subjects, the combination of the hippocampus, the amygdala, and the ventricle would likely yield an optimal LDA classifier. According to the leave-one-out cross-validation procedure, as described in Figure 3, the correct classification rates were: 88% for the HC group, 86% for the AD group, and 86% for the two groups together. In comparison, the correct

classification rates using volume information, via the same procedure, were: 76% for the HC group, 75% for the AD group, and 75% for the two groups in overall.

Comparisons of MCI-Stable and MCI-AD

To compare the two subtypes of MCI at baseline: MCI that remained stable (MCI-stable) and MCI that deteriorated to AD (MCI-AD), we performed the same vertex-based statistical analysis for all the seven structures in both hemispheres. Vertices on the template surfaces revealing statistically significant group differences are shown in Figures 16 to 18. Comparing MCI-stable versus MCI-AD, we found group surface differences in three structures: the hippocampus, the amygdala, and the lateral ventricle. Little difference has been detected on other subcortical structures. The shape variations between MCI-stable and MCI-AD, in terms of the subregions of left amygdala and the hippocampus in both hemispheres, are displayed in Figures 19 and 20.

DISCUSSION

Statistical shape analysis offers an alternative to volume-based analysis for detecting and quantifying abnormalities of deep subcortical and ventricular structures in dementia of the Alzheimer type. An analysis of the surfaces enclosing the brain structures allows for the characterization of shape abnormalities that are associated with MCI or AD, which do not necessarily involve changes in the overall size of the structures. In addition to measuring group differences in subjects with MCI or AD compared with HC ones, shape-based analysis may also help identifying MCI individuals who are suffering from prodromal AD [McEvoy and Brewer, 2010; Morris and Cummings, 2005]. Existing shape analysis methods have mainly focused on a single structure such as hippocampus [Ferrarini et al., 2006; Thompson et al., 2004; Wang et al., 2003, 2006], whereas our study included all the subcortical structures and the lateral ventricle. The shape abnormality of a single structure may be nonspecific to AD. Thus, a combination of neuroimaging measures from multiple structures may be more sensitive and specific to AD pathology, helping identify abnormalities in MCI and AD and predicting conversion from MCI to AD more accurately. According to our discriminant analysis results, combining the shape information of the three structures—amygdala, hippocampus, and lateral ventricle improved both the sensitivity and the specificity obtained from any single structure. The highest specificity and sensitivity from a single structure is 86% and 81% from the hippocampus. These two numbers were increased to 88% and 86% by using the shape measures from those three structures. This study is an extension and enrichment of the study reported in Qiu et al. [2009]. The procedures of surface generation, surface template estimation, and surface mapping are similar to those introduced in [Qiu et al., 2009]. Other methods of creating surfaces with topology correction from volume segmentations are available [Bazin and Pham, 2007; Brechbuhler et al., 1995; Han et al., 2003; Shi et al., 2010], the investigation of which will be one important future direction of our work. This study differs from the one by [Qiu et al., 2009] in several aspects: First, the analysis methods are different in that, [Qiu et al., 2009] introduced the Laplace-Beltrami (LB) operator on the template surfaces and then performed random field testing on the LB coefficients of multiple structures whereas we constructed a statistical model directly on the log-determinant of the Jacobian of the deformation maps

and utilized PCA on the initial momenta vectors to discriminate between the HC and AD groups. Second, compared with the results reported in [Qiu et al., 2009], our method detected much stronger shape differences between different groups. Also, the results are slightly different since we found no atrophy in lateral ventricle in either side and no expansion in either hippocampus or amygdala in both hemispheres. In contrast, according to the results shown in [Qiu et al., 2009], mild expansion was found in the posterior segment of the hippocampus and some regions on amygdala in both hemispheres. Mild atrophy was also reported between MCI and AD in the posterior horn of the bilateral lateral ventricles. Third, instead of only evaluating the differences that exist in MCI and AD, we also applied our method to differentiate the subtypes of MCI based on baseline measures. Moreover, we explored more subtle structural abnormalities by subdividing the hippocampus at each side into CA1, subiculum, and the remaining part consisting of CA2, CA3, and dentate gyrus, the left amygdala into basolateral, basomedial, centromedial, and lateral nucleus. Finally, about twice as many MR scans have been used in our study.

Our study revealed significant atrophy in the hippocampus and the amygdala and prominent expansion in the lateral ventricle, in both hemispheres, in MCI as well as AD groups (Figs. 6–8), which suggested that histopathological changes occurred before being defined as AD clinically. This conclusion is consistent with previous findings [Fennema- Morra et al., 2009; Notestine et al., 2009; Qiu et al., 2009]. Transferring the subregions of the hippocampus, both left and right, from a 0.8 mm isotropic 7.0T MR scan onto our template surfaces (Figs. 13 and 14) suggested that the most pronounced atrophy occurred in the subregion CA1, which has been reported to be associated with memory and learning [Lepage et al., 1998; Markesbery et al., 2006; Price et al., 2001; West et al., 2004]. The subregions revealing the strongest atrophy in either MCI or AD populations on the left amygdala were found to be close to the basolateral complex (Fig. 12), the region that has also been reported to play a role in modulating consolidation of memory [Vazdarjanova and McGaugh, 1999]. According to [Price, 2003], the amygdala can be parcellated into core and noncore subregions based on functional characteristics. The core region consists of the lateral, basal, and accessory basal nuclei while the non-core region consists of the remaining central, medial, and cortex nuclei [Munn et al., 2007; Sheline et al., 1998]. The fact that relatively stronger shape compression was detected at basolateral and lateral nucleus, compared with the other two subregions, is plausible because these two regions are core regions that are responsible for storing the memories of emotion.

There have been extensive studies on hippocampal shape analysis in comparing healthy controls with AD populations [Csernansky et al., 2000, 2005; Li et al., 2007; Scher et al., 2007; Wang et al., 2003, 2006]. The general conclusions have been that there is atrophy near CA regions, which is in agreement with our findings on the hippocampus. However, some studies revealed no group differences in the right hippocampus [Csernansky et al., 2005]. One potential limitation of those earlier studies is that the sample size was limited. For example, the largest study conducted by [Wang et al., 2006] compared 49 cases with minimal AD to 86 normal controls. The sample size of our study (210 HC, 369 MCI, 175 AD) is large for this kind of analysis, which may be an explanation for our stronger results. For interpreting the role of the amygdala in MCI and AD, there are relatively few neuroimaging studies [Poulin et al., 2011], despite that there are quite a few earlier

histopathological findings on it [Herzog and Kemper, 1980; Scott et al., 1991, 1992; Tsuchiya and Kosaka, 1990]. The nonuniform shape changes along the amygdala may well explain the variation of volume detected in [Poulin et al., 2011]. Our results in the lateral regions of the left amygdala coincide with the findings presented in [Cavedo et al., 2011; Qiu et al., 2009].

In addition to structural abnormalities near the medial temporal area and the lateral ventricle, we also found mild regional atrophy of basal ganglia structures such as the left and right putamen and globus pallidus in MCI and AD groups (Fig. 9). Either atrophy or expansion has been detected on some vertices of the surfaces of thalamus at each side in MCI and AD, compared with HC (Fig. 9). Mild expansion was also found in caudate nucleus in AD when compared with normal healthy subjects (Fig. 9). Since the number of vertices showing expansion on the caudate surface is very small, this may not influence the overall volume size, which makes it difficult to measure via the overall structure volume. Also, the expansion in either caudate or thalamus may be due to inaccurate automated volumetric segmentations or partial volume effects. As revealed by Figure 9, most expansion in the caudate nucleus occurs at the tail part. This part of the caudate has been suggested to be the most difficult region to segment even manually since the contrast decreases a lot in 3T T1-weighted images between the caudate tail and its surrounding white matter. We examined the original segmentation from FreeSurfer around this region in representative scans. As shown in Figure 21, the original automated segmentation inaccurately labeled the tail part of the caudate, which could be a potential cause for the unexpected expansion in the AD group when compared with the other two groups. Further application of the same statistical shape analysis pipeline on the manually-labeled caudate may help address this issue. Comparing MCI and AD, we found a similar pattern but much stronger magnitude of atrophy or expansion in AD, which indicates that the severity of regional shape changes (atrophy or expansion) is associated with the degree of clinical impairment. This finding has also been reported for cortical regions [Dickerson et al., 2009; McDonald et al., 2009].

The purpose of comparing the baseline measures of the subgroups of MCI is to help assess whether a person diagnosed with MCI has underlying AD pathophysiology based only on baseline information. In our datasets, among the subjects that had been diagnosed as MCI at baseline, 205 were diagnosed to have remained MCI (MCI-stable), while another 151 converted to AD (MCI-AD) over a fixed follow-up time of 1 year. Unlike the significant differences observed among HC, MCI, and AD groups in basal ganglia and thalamus, the MCI subgroups did not significantly differ in these structures. Compared with MCI individuals that did not deteriorate to AD, atrophy in both hippocampus and amygdala and regional expansion of lateral ventricle in both hemispheres was detected in MCI-AD (Figs. 16–18). According to the subsegmentations of the hippocampus, the strongest shape changes also occurred at CA1 in both hemispheres (Fig. 20). For the left amygdala, the basolateral subregion was found to display most prominent atrophy in MCI-AD (Fig. 19), as compared with MCI-stable.

According to the *p*-values shown in Table III, the PCA-based method is capable of capturing even the mild differences between two groups, demonstrating results consistent with those obtained from the vertex-based analyses. As suggested in [Wang et al., 2007], our PCA-

based method may provide a good way to find a biomarker for discriminating healthy subjects from the subjects with MCI or AD. Our initial discriminant analysis suggests that the shape information associated with each individual structure is consistently more discriminating than the corresponding volume information. A direct comparison shown in Table IV suggests that, for each single structure, utilizing its shape information for LDA discrimination would improve the classification rates obtained by utilizing the volume information. We tested on all the combinations of the PCs from all the structures to select the optimal LDA classifier in the leave-one-out procedure. Our procedure yielded correct classification rates of 88% for the HC group and 86% for the AD group. Among all the optimal LDA classifiers, hippocampus has been selected for 88% of the time, amygdala 83% of the time, ventricle 71% of the time. This conclusion agrees with our vertex based analysis results in which we found that the most prominent shape variations occurred at these three structures.

In this study, the shape PCs were computed for each structure separately instead of being computed at once for all the structures. The main concern of not performing PCA on features from all the seven structures simultaneously is that it may downplay some small but important structures such as the amygdala. Extracting features from multiple structures at once should be considered in future work, as done in [Gorczowski et al., 2010]. In finding the optimal LDA classifier, we considered the set of PCs from each structure as a unit and then did a cross-validation search for all the possible combinations. It is plausible that we may get even better classification results if we use a combination of a subset of the PCs of one structure and a subset of the PCs of some other structures. However, considering each PC separately would be computationally prohibitive. A possible solution can be to boost the LDA and select the most relevant PCs at each boosting iteration [Flores et al., 2010; Lu et al., 2006; Skurichina and Duin, 2002]. This will be the subject of future work.

Our present study was mainly focused on analyzing the shape differences of seven structures (left and right), as well as the three subregions of hippocampus and the four subregions of left amygdala, in groups of different disease states (HC, MCI, AD). In addition, we applied our method to study the shape differences within the MCI group, in an attempt to identify regional changes in subjects with MCI that converted to AD over time. We have also presented our preliminary results in developing biomarkers from shape information of those structures that can predict risk of decline. The biomarker, designed from the initial momentum information of the seven subcortical structures, is relatively novel compared with the biomarker proposed by other studies. Currently, a lot of studies have been focusing on identifying biomarkers for the classification of AD/HC based on structural MRI features such as the hippocampus volume and the cortical thickness [Cho et al., 2011; Desikan et al., 2009; Klöppel et al., 2008; Shen et al., 2011; Vemuri et al., 2008]. Future work should focus on incorporating the shape information of multiple cortical regions to aid the discrimination procedure as well as utilizing more advanced machine learning techniques beyond LDA for the analysis. In addition, incorporating the subsegmentations of the hippocampus and the amygdala should advance the classification in AD/MCI as demonstrated in [Li et al., 2007]. Another important extension is to incorporate longitudinal information by analyzing the subcortical structures on serial structure images to determine whether these methods are

valuable for tracking disease progression and predicting AD conversion from MCI or HC subjects.

Acknowledgments

The authors thank Pamela Belmonte-Mahon for collecting the two 7T scans. The authors also thank Thi Lan Huong for manually segmenting the left amygdala and the hippocampi into subregions. ADNI data are disseminated by the Laboratory for Neuro Imaging at the University of California, Los Angeles. Anders M. Dale is a founder and holds equity in CorTechs Labs, Inc., and also serves on its Scientific Advisory Board. Michael I. Miller owns an equal share in Anatomyworks LLC. The terms of this arrangement have been reviewed and approved by the Johns Hopkins University as well as the University of California, San Diego in accordance with their conflict of interest policies.

Contract grant sponsor: NIH; Contract grant number: R01 EB000975, NIH P41 RR15241, R01 EB008171, P30 AG010129, and K01 AG030514; Contract grant sponsor: Alzheimer's Disease Neuroimaging Initiative (ADNI) (National Institutes of Health); Contract grant number: U01 AG024904; Contract grant sponsor: National Institute on Aging, the National Institute of Biomedical Imaging and Bioengineering, Abbott; Alzheimer's Association, Alzheimer's Drug Discovery Foundation, Amorfix Life Sciences Ltd., AstraZeneca, Bayer HealthCare, BioClinica, Inc., Biogen Idec Inc., Bristol-Myers Squibb Company, Eisai Inc., Elan Pharmaceuticals Inc., Eli Lilly and Company, F. Hoffmann-La Roche Ltd. and its affiliated company Genentech, Inc., GE Healthcare, Innoge-netics, N.V., IXICO Ltd., Janssen Alzheimer Immunotherapy Research & Development, LLC., Johnson & Johnson Pharmaceutical Research & Development LLC., Medpace, Inc., Merck & Co., Inc., Meso Scale Diagnostics, LLC., Novartis Pharmaceuticals Corporation, Pfizer Inc., Servier, Synarc Inc., Takeda Pharmaceutical Company, Canadian Institutes of Health Research, Foundation for the National Institutes of Health (www.fnih.org), Contract grant sponsor: Northern California Institute for Research and Education, and Alzheimer's Disease Cooperative Study at the University of California, San Diego.

References

Anderson, TW. An Introduction to Multivariate Statistical Analysis. New York: Wiley; 1958.

Apostolova LG, Dinov ID, Dutton RA, Hayashi KM, Toga AW, Cummings JL, Thompson PM. 3D comparison of hippocampal atrophy in amnestic mild cognitive impairment and Alzheimer's disease. Brain. 2006; 129:2867–2873. [PubMed: 17018552]

Ashburner J, Friston KJ. Voxel-based morphometry—The methods. Neuroimage. 2000; 11:805–821. [PubMed: 10860804]

Atiya M, Hyman BT, Albert MS, Killiany R. Structural magnetic resonance imaging in established and prodromal Alzheimer disease: A review. Alzheimer Dis Assoc Disord. 2003; 17:177–195. [PubMed: 14512832]

Barnes J, Bartlett JW, van de Pol LA, Loy CT, Scahill RI, Frost C, Thompson P, Fox NC. A meta-analysis of hippocampal atrophy rates in Alzheimer's disease. Neurobiol Aging. 2009; 30:1711–1723. [PubMed: 18346820]

Bazin P, Pham DL. Topology correction of segmented medical images using a fast marching algorithm. Comput Methods Programs Biomed. 2007; 88:182–190. [PubMed: 17942182]

Bell-McGinty S, Butters MA, Meltzer CC, Greer PJ, Reynolds CF III, Becker JT. Brain morphometric abnormalities in geriatric depression: long-term neurobiological effects of illness duration. Am J Psychiatry. 2002; 159:1424–1427. [PubMed: 12153839]

Brechbühler C, Gerig G, Kübler O. Parametrization of closed surfaces for 3-D shape description. Comput Vision Image Understanding. 1995; 61:154–170.

Buckner RL, Head D, Parker J, Fotenos AF, Marcus D, Morris JC, Snyder AZ. A unified approach for morphometric and functional data analysis in young, old, and demented adults using automated atlas-based head size normalization: Reliability and validation against manual measurement of total intracranial volume. Neuroimage. 2004; 23:724–738. [PubMed: 15488422]

Camion, V.; Younes, L. Geodesic Interpolating Splines. In: Figueiredo, MAT.; Zerubia, J.; Jain, AK., editors. EMMCVPR 2001, Vol. 2134 of Lecture Notes in Computer Sciences. Springer-Verlag; 2001. p. 513-527.

Cavedo E, Boccardi M, Ganzola R, Canu E, Beltramello A, Caltagirone C, Thompson PM, Frisoni GB. Local amygdala structural differences with 3T MRI in patients with Alzheimer disease. Neurology. 2011; 76:727–733. [PubMed: 21339500]

Ceritoglu C, Oishi K, Li X, Chou MC, Younes L, Albert M, Lyketsos C, van Zijl PC, Miller MI, Mori S. Multi-contrast large deformation diffeomorphic metric mapping for diffusion tensor imaging. Neuroimage. 2009; 47:618–627. [PubMed: 19398016]

Chetelat G, Baron JC. Early diagnosis of Alzheimer's disease: Contribution of structural neuroimaging. Neuroimage. 2003; 18:525–41. [PubMed: 12595205]

Chiang M, Dutton RA, Hayashi KM, Lopez OL, Aizenstein HJ, Toga AW, Becker JT, Thompson PM. 3D pattern of brain atrophy in HIV/AIDS visualized using tensor-based morphometry. Neuroimage. 2007; 34:44–60. [PubMed: 17035049]

Cho Y, Seong J, Jeong Y, Shin SY. Individual subject classification for Alzheimer's disease based on incremental learning using a spatial frequency representation of cortical thickness data. Neuroimage. 2011; 59:2217–2230. [PubMed: 22008371]

Convit A, de Asis J, de Leon MJ, Tarshish CY, De Santi S, Rusinek H. Atrophy of the medial occipitotemporal, inferior, and middle temporal gyri in non-demented elderly predict decline to Alzheimer's disease. Neurobiol Aging. 2000; 21:19–26. [PubMed: 10794844]

Csernansky JG, Joshi S, Wang L, Haller JW, Gado M, Miller JP, Grenander U, Miller MI. Hippocampal morphometry in schizophrenia by high dimensional brain mapping. Proc Natl Acad Sci USA. 1998; 95:11406–11411. [PubMed: 9736749]

Csernansky JG, Wang L, Jones D, Rastogi-Cruz D, Posener JA, Heydebrand G, Miller JP, Miller MI. Hippocampal deformities in schizophrenia characterized by high dimensional brain mapping. Am J Psychiatry. 2002; 159:2000–2006. [PubMed: 12450948]

Csernansky JG, Wang L, Joshi S, Miller JP, Gado M, Kido D, McKeel D, Morris JC, Miller MI. Early DAT is distinguished from aging by high-dimensional mapping of the hippocampus. Dementia of the Alzheimer type. Neurology. 2000; 55:1636–1643. [PubMed: 11113216]

Csernansky JG, Wang L, Swank J, Miller JP, Gado M, McKeel D, Miller MI, Morris JC. Preclinical detection of Alzheimer's disease: Hippocampal shape and volume predict dementia onset in the elderly. Neuroimage. 2005; 25:783–792. [PubMed: 15808979]

de Jong LW, van der Hiele K, Veer IM, Houwing JJ, Westendorp RG, Bollen EL, de Bruin PW, Middelkoop HA, van Buchem MA, van der Grond J. Strongly reduced volumes of putamen and thalamus in Alzheimer's disease: An MRI study. Brain. 2008; 131:3277–3285. [PubMed: 19022861]

Dempster AP, Laird NM, Rubin DB. Maximum Likelihood from Incomplete Data via the EM Algorithm. J R Stat Soc Ser B. 1977; 39:1–38.

Desikan RS, Cabral HJ, Hess CP, Dillon WP, Glastonbury CM, Weiner MW, Schmansky NJ, Greve DN, Salat DH, Buckner RL. Automated MRI measures identify individuals with mild cognitive impairment and Alzheimer's disease. Brain. 2009; 132:2048–2057. [PubMed: 19460794]

Dickerson BC, Bakkour A, Salat DH, Feczko E, Pacheco J, Greve DN, Grodstein F, Wright CI, Blacker D, Rosas HD, Sperling RA, Atri A, Growdon JH, Hyman BT, Morris JC, Fischl B, Buckner RL. The cortical signature of Alzheimer's disease: Regionally specific cortical thinning relates to symptom severity in very mild to mild AD dementia and is detectable in asymptomatic amyloid-positive individuals. Cereb Cortex. 2009; 19:497–510. [PubMed: 18632739]

Dickerson BC, Goncharova I, Sullivan MP, Forchetti C, Wilson RS, Bennett DA, Beckett LA, deToledo-Morrell L. MRI-derived entorhinal and hippocampal atrophy in incipient and very mild Alzheimer's disease. Neurobiol Aging. 2001; 22:747–754. [PubMed: 11705634]

Dupuis P, Grenander U, Miller MI. Variational problems on flows of diffeomorphisms for image matching. Q Appl Math. 1998; 56:587–600.

Fennema-Notestine C, Hagler DJ Jr, McEvoy LK, Fleisher AS, Wu EH, Karow DS, Dale AM. Alzheimer's Disease Neuroimaging Initiative. Structural MRI biomarkers for preclinical and mild Alzheimer's disease. Hum Brain Mapp. 2009; 30:3238–3253. [PubMed: 19277975]

Ferrarini L, Palm WM, Olofsen H, van Buchem MA, Reiber JH, Admiraal-Behloul F. Shape differences of the brain ventricles in Alzheimer's disease. Neuroimage. 2006; 32:1060–1069. [PubMed: 16839779]

Ferri CP, Prince M, Brayne C, Brodaty H, Fratiglioni L, Ganguli M, Hall K, Hasegawa K, Hendrie H, Huang Y, Jorm A, Mathers C, Menezes PR, Rimmer E, Scazufca M. Alzheimer's Disease International. Global prevalence of dementia: A Delphi consensus study. Lancet. 2005; 366:2112–2117. [PubMed: 16360788]

Fischl B, Salat DH, Busa E, Albert M, Dieterich M, Haselgrove C, van der Kouwe A, Killiany R, Kennedy D, Klaveness S, Montillo A, Makris N, Rosen B, Dale AM. Whole brain segmentation: Automated labeling of neuroanatomical structures in the human brain. Neuron. 2002; 33:341–355. [PubMed: 11832223]

Flores, A.; Linguraru, MG.; Okada, K. Boosted-LDA for biomedical data analysis. International Workshop on Machine Learning in Medical Imaging (MLMI)—In conjunction with MICCAI; September 20, 2010; 2010.

Frisoni GB, Caroli A. Neuroimaging outcomes for clinical trials. J Nutr Health Aging. 2007; 11:348–352. [PubMed: 17653497]

Fukutani Y, Kobayashi K, Nakamura I, Watanabe K, Isaki K, Cairns NJ. Neurons, intracellular and extracellular neurofibrillary tangles in subdivisions of the hippocampal cortex in normal ageing and Alzheimer's disease. Neurosci Lett. 1995; 200:57–60. [PubMed: 8584267]

Gauthier S, Reisberg B, Zaudig M, Petersen RC, Ritchie K, Broich K, Belleville S, Brodaty H, Bennett D, Chertkow H, Cummings JL, de Leon M, Feldman H, Ganguli M, Hampel H, Scheltens P, Tierney MC, Whitehouse P, Winblad B. International Psychogeriatric Association Expert Conference on mild cognitive impairment. Mild cognitive impairment. Lancet. 2006; 367:1262–1270. [PubMed: 16631882]

Gorczowski K, Styner M, Jeong Ja Yeon, Marron JS, Piven J, Hazlett HC, Pizer SM, Gerig G. Multi-object analysis of volume, pose, and shape using statistical discrimination. IEEE Trans Pattern Anal Mach Intell. 2010; 32:652–661. [PubMed: 20224121]

Han X, Xu C, Prince JL. A topology preserving level set method for geometric deformable models. IEEE Trans Pattern Anal Mach Intell. 2003; 25:755–768.

Helm PA, Younes L, Beg MF, Ennis DB, Leclercq C, Faris OP, McVeigh E, Kass D, Miller MI, Winslow RL. Evidence of structural remodeling in the dyssynchronous failing heart. Circ Res. 2006; 98:125–132. [PubMed: 16339482]

Henneman WJ, Sluimer JD, Barnes J, van der Flier WM, Sluimer IC, Fox NC, Scheltens P, Vrenken H, Barkhof F. Hippocampal atrophy rates in Alzheimer disease: Added value over whole brain volume measures. Neurology. 2009; 72:999–1007. [PubMed: 19289740]

Herzog AG, Kemper TL. Amygdaloid changes in aging and dementia. Arch Neurol. 1980; 37:625–629. [PubMed: 7425886]

Holland D, Brewer JB, Hagler DJ, Fennema-Notestine C, Dale AM. Alzheimer's Disease Neuroimaging Initiative. Subregional neuroanatomical change as a biomarker for Alzheimer's disease. Proc Natl Acad Sci USA. 2009; 106:20954–20959. [PubMed: 19996185]

Holland D, McEvoy LK, Dale AM. the Alzheimer's Disease Neuroimaging Initiative. Unbiased comparison of sample size estimates from longitudinal structural measures in ADNI. Hum Brain Mapp. 2011; 33:2586–2602. [PubMed: 21830259]

Holland D, McEvoy LK, Desikan RS, Dale AM. Alzheimer's Disease Neuroimaging Initiative. Enrichment and stratification for predementia Alzheimer disease clinical trials. PLoS One. 2012; 7:e47739. [PubMed: 23082203]

Jack CR Jr, Lowe VJ, Weigand SD, Wiste HJ, Senjem ML, Knopman DS, Shiung MM, Gunter JL, Boeve BF, Kemp BJ, Weiner M, Petersen RC. Alzheimer's Disease Neuroimaging Initiative. Serial PIB and MRI in normal, mild cognitive impairment and Alzheimer's disease: implications for sequence of pathological events in Alzheimer's disease. Brain. 2009; 132:1355–1365. [PubMed: 19339253]

Jack CR Jr, Petersen RC, Xu YC, O'Brien PC, Smith GE, Ivnik RJ, Boeve BF, Waring SC, Tangalos EG, Kokmen E. Prediction of AD with MRI-based hippocampal volume in mild cognitive impairment. Neurology. 1999; 52:1397–1403. [PubMed: 10227624]

Joshi SC, Miller MI. Landmark matching via large deformation diffeomorphisms. IEEE Trans Image Process. 2000; 9:1357–1370. [PubMed: 18262973]

Jovicich J, Czanner S, Greve D, Haley E, van der Kouwe A, Gollub R, Kennedy D, Schmitt F, Brown G, Macfall J, Fischl B, Dale A. Reliability in multi-site structural MRI studies: Effects of gradient non-linearity correction on phantom and human data. Neuroimage. 2006; 30:436–443. [PubMed: 16300968]

Killiany RJ, Hyman BT, Gomez-Isla T, Moss MB, Kikinis R, Jolesz F, Tanzi R, Jones K, Albert MS. MRI measures of entorhinal cortex vs hippocampus in preclinical AD. Neurology. 2002; 58:1188–1196. [PubMed: 11971085]

Klöppel S, Stonnington CM, Chu C, Draganski B, Scahill RI, Rohrer JD, Fox NC, Jack CR, Ashburner J, Frackowiak RS. Automatic classification of MR scans in Alzheimer's disease. Brain. 2008; 131:681–689. [PubMed: 18202106]

Landis JR, Koch GG. The measurement of observer agreement for categorical data. Biometrics. 1977; 33:159–174. [PubMed: 843571]

Larrieu S, Letenneur L, Orgogozo JM, Fabrigoule C, Amieva H, Le Carret N, Barberger-Gateau P, Dartigues JF. Incidence and outcome of mild cognitive impairment in a population-based prospective cohort. Neurology. 2002; 59:1594–1599. [PubMed: 12451203]

Lepage M, Habib R, Tulving E. Hippocampal PET activations of memory encoding and retrieval: the HIPER model. Hippocampus. 1998; 8:313–322. [PubMed: 9744418]

Li S, Shi F, Pu F, Li X, Jiang T, Xie S, Wang Y. Hippocampal shape analysis of Alzheimer disease based on machine learning methods. AJNR Am J Neuroradiol. 2007; 28:1339–1345. [PubMed: 17698538]

Lu J, Plataniotis K, Venetsanopoulos A, Li SZ. Ensemble-based discriminant learning with boosting for face recognition. IEEE Trans Neural Netw. 2006; 17:166–178. [PubMed: 16526485]

Ma J, Miller MI, Younes L. A bayesian generative model for surface template estimation. Int J Biomed Imaging. 2010; 2010:974957. [PubMed: 20885934]

Madsen SK, Ho AJ, Hua X, Saharan PS, Toga AW, Jack CR Jr, Weiner MW, Thompson PM. 3D maps localize caudate nucleus atrophy in 400 Alzheimer's disease, mild cognitive impairment, and healthy elderly subjects. Neurobiol Aging. 2010; 31:1312–1325. [PubMed: 20538376]

Markesbery WR, Schmitt FA, Kryscio RJ, Davis DG, Smith CD, Wekstein DR. Neuropathologic substrate of mild cognitive impairment. Arch Neurol. 2006; 63:38–46. [PubMed: 16401735]

McDonald CR, McEvoy LK, Gharapetian L, Fennema-Notestine C, Hagler DJ Jr, Holland D, Koyama A, Brewer JB, Dale AM. Alzheimer's Disease Neuroimaging Initiative. Regional rates of neocortical atrophy from normal aging to early Alzheimer disease. Neurology. 2009; 73:457–465. [PubMed: 19667321]

McEvoy LK, Brewer JB. Quantitative structural MRI for early detection of Alzheimer's disease. Expert Rev Neurother. 2010; 10:1675–1688. [PubMed: 20977326]

McKhann G, Drachman D, Folstein M, Katzman R, Price D, Stadlan EM. Clinical diagnosis of Alzheimer's disease: Report of the NINCDS-ADRDA Work Group under the auspices of Department of Health and Human Services Task Force on Alzheimer's Disease. Neurology. 1984; 34:939–944. [PubMed: 6610841]

Miller MI, Trouve A, Younes L. On the metrics and euler-lagrange equations of computational anatomy. Annu Rev Biomed Eng. 2002; 4:375–405. [PubMed: 12117763]

Miller MI, Trouve A, Younes L. Geodesic shooting for computational anatomy. J Math Imaging Vis. 2006; 24:209–228. [PubMed: 20613972]

Morra JH, Tu Z, Apostolova LG, Green AE, Avedissian C, Madsen SK, Parikshak N, Hua X, Toga AW, Jack CR Jr, Schuff N, Weiner MW, Thompson PM. Alzheimer's Disease Neuroimaging Initiative. Automated 3D mapping of hippocampal atrophy and its clinical correlates in 400 subjects with Alzheimer's disease, mild cognitive impairment, and elderly controls. Hum Brain Mapp. 2009; 30:2766–2788. [PubMed: 19172649]

Morris JC, Cummings J. Mild cognitive impairment (MCI) represents early-stage Alzheimer's disease. J Alzheimers Dis. 2005; 7:235–239. discussion 255–262. [PubMed: 16006667]

Morris JC, Storandt M, Miller JP, McKeel DW, Price JL, Rubin EH, Berg L. Mild cognitive impairment represents early-stage Alzheimer disease. Arch Neurol. 2001; 58:397–405. [PubMed: 11255443]

Munn MA, Alexopoulos J, Nishino T, Babb CM, Flake LA, Singer T, Ratnanather JT, Huang H, Todd RD, Miller MI, Botteron KN. Amygdala volume analysis in female twins with major depression. Biol Psychiatry. 2007; 62:415–422. [PubMed: 17511971]

Nichols T, Hayasaka S. Controlling the familywise error rate in functional neuroimaging: A comparative review. Stat Methods Med Res. 2003; 12:419–446. [PubMed: 14599004]

Poulin SP, Dautoff R, Morris JC, Barrett LF, Dickerson BC. Alzheimer's Disease Neuroimaging Initiative. Amygdala atrophy is prominent in early Alzheimer's disease and relates to symptom severity. Psychiatry Res. 2011; 194:7–13. [PubMed: 21920712]

Price JL. Comparative aspects of amygdala connectivity. Ann NY Acad Sci. 2003; 985:50–58. [PubMed: 12724147]

Price JL, Ko AI, Wade MJ, Tsou SK, McKeel DW, Morris JC. Neuron number in the entorhinal cortex and CA1 in preclinical Alzheimer disease. Arch Neurol. 2001; 58:1395–1402. [PubMed: 11559310]

Qiu A, Brown T, Fischl B, Kolasny A, Ma J, Buckner R, Miller MI. Atlas generation for subcortical and ventricular structures with its applications in shape analysis. IEEE Trans Image Process. 2010; 19:1539–1547. [PubMed: 20129863]

Qiu A, Younes L, Wang L, Ratnanather JT, Gillepsie SK, Kaplan G, Csernansky J, Miller MI. Combining anatomical manifold information via diffeomorphic metric mappings for studying cortical thinning of the cingulate gyrus in schizophrenia. Neuroimage. 2007; 37:821–833. [PubMed: 17613251]

Qiu A, Miller MI. Multi-structure network shape analysis via normal surface momentum maps. Neuroimage. 2008; 42:1430. [PubMed: 18675553]

Qiu A, Fennema-Notestine C, Dale AM, Miller MI. Alzheimer's Disease Neuroimaging Initiative. Regional shape abnormalities in mild cognitive impairment and Alzheimer's disease. Neuroimage. 2009; 45:656–661. [PubMed: 19280688]

Qiu A, Younes L, Miller MI, Csernansky JG. Parallel transport in diffeomorphisms distinguishes the time-dependent pattern of hippocampal surface deformation due to healthy aging and the dementia of the Alzheimer's type. Neuroimage. 2008; 40:68–76. [PubMed: 18249009]

Ramani A, Jensen JH, Helpern JA. Quantitative MR imaging in Alzheimer disease. Radiology. 2006; 241:26–44. [PubMed: 16990669]

Rangarajan, A.; Chui, H.; Bookstein, F. Information Processing in Medical Imaging (IPMI). Springer; Berlin: 1997. The softassign Procrustes matching algorithm; p. 29-42.

Ridha BH, Anderson VM, Barnes J, Boyes RG, Price SL, Rossor MN, Whitwell JL, Jenkins L, Black RS, Grundman M, Fox NC. Volumetric MRI and cognitive measures in Alzheimer disease: comparison of markers of progression. J Neurol. 2008; 255:567–574. [PubMed: 18274807]

Scher AI, Xu Y, Korf ES, White LR, Scheltens P, Toga AW, Thompson PM, Hartley SW, Witter MP, Valentino DJ, Launer LJ. Hippocampal shape analysis in Alzheimer's disease: A population-based study. Neuroimage. 2007; 36:8–18. [PubMed: 17434756]

Scott SA, DeKosky ST, Scheff SW. Volumetric atrophy of the amygdala in Alzheimer's disease: Quantitative serial reconstruction. Neurology. 1991; 41:351–356. [PubMed: 2006000]

Scott SA, DeKosky ST, Sparks DL, Knox CA, Scheff SW. Amygdala cell loss and atrophy in Alzheimer's disease. Ann Neurol. 1992; 32:555–563. [PubMed: 1456740]

Sheline YI, Gado MH, Price JL. Amygdala core nuclei volumes are decreased in recurrent major depression. Neuroreport. 1998; 9:2023–2028. [PubMed: 9674587]

Shen, L.; Kim, S.; Qi, Y.; Inlow, M.; Swaminathan, S.; Nho, K.; Wan, J.; Risacher, S.; Shaw, L.; Trojanowski, J. Identifying neuroimaging and proteomic biomarkers for MCI and AD via the elastic net. In: Liu, T.; Shen, D.; Ibanez, L.; Tao, X., editors. MBIA 2011 LNCS. Vol. 7012. Springer; Heidelberg: 2011. p. 27-34.

Shi Y, Lai R, Morra JH, Dinov I, Thompson PM, Toga AW. Robust surface reconstruction via Laplace-Beltrami Eigen-projection and boundary deformation. IEEE Trans Med Imaging. 2010; 29:2009–2022. [PubMed: 20624704]

Skurichina M, Duin RP. Bagging, boosting and the random subspace method for linear classifiers. Pattern Anal Appl. 2002; 5:121–135.

Sled JG, Zijdenbos AP, Evans AC. A nonparametric method for automatic correction of intensity nonuniformity in MRI data. IEEE Trans Med Imaging. 1998; 17:87–97. [PubMed: 9617910]

Sluimer JD, van der Flier WM, Karas GB, van Schijndel R, Barnes J, Boyes RG, Cover KS, Olabarriaga SD, Fox NC, Scheltens P, Vrenken H, Barkhof F. Accelerating regional atrophy rates in the progression from normal aging to Alzheimer's disease. Eur Radiol. 2009; 19:2826–2833. [PubMed: 19618189]

Small SA, Nava AS, Perera GM, Delapaz R, Stern Y. Evaluating the function of hippocampal subregions with high-resolution MRI in Alzheimer's disease and aging. Microsc Res Tech. 2000; 51:101–108. [PubMed: 11002358]

Thompson PM, Hayashi KM, De Zubicaray GI, Janke AL, Rose SE, Semple J, Hong MS, Herman DH, Gravano D, Doddrell DM, Toga AW. Mapping hippocampal and ventricular change in Alzheimer disease. Neuroimage. 2004; 22:1754–1766. [PubMed: 15275931]

Tsuchiya K, Kosaka K. Neuropathological study of the amygdala in presenile Alzheimer's disease. J Neurol Sci. 1990; 100:165–173. [PubMed: 2089133]

Vaillant M, Miller MI, Younes L, Trouve A. Statistics on diffeomorphisms via tangent space representations. Neuroimage. 2004; 23(Suppl 1):S161–S169. [PubMed: 15501085]

Vaillant, M.; Glaunès, J. Surface matching via Currents. In: Christensen, G.; Sonka, M., editors. Information Processing in Medical Imaging. Lecture notes in computer sciences. New York: Springer-Verlag; 2005. p. 381-392.

van de Pol LA, Hensel A, van der Flier WM, Visser P, Pijnenburg YAL, Barkhof F, Gertz HJ, Scheltens P. Hippocampal atrophy on MRI in frontotemporal lobar degeneration and Alzheimer's disease. J Neurol Neurosurg Psychiatry. 2006; 77:439–442. [PubMed: 16306153]

Vazdarjanova A, McGaugh JL. Basolateral amygdala is involved in modulating consolidation of memory for classical fear conditioning. J Neurosci. 1999; 19:6615–6622. [PubMed: 10414989]

Vemuri P, Gunter JL, Senjem ML, Whitwell JL, Kantarci K, Knopman DS, Boeve BF, Petersen RC, Jack CR Jr. Alzheimer's disease diagnosis in individual subjects using structural MR images: Validation studies. Neuroimage. 2008; 39:1186–1197. [PubMed: 18054253]

Visser PJ, Scheltens P, Verhey FR, Schmand B, Launer LJ, Jolles J, Jonker C. Medial temporal lobe atrophy and memory dysfunction as predictors for dementia in subjects with mild cognitive impairment. J Neurol. 1999; 246:477–485. [PubMed: 10431775]

Wang Y, Song Y, Rajagopalan P, An T, Liu K, Chou Y, Gutman B, Toga AW, Thompson PM. Surface-based TBM boosts power to detect disease effects on the brain: An N= 804 ADNI study. Neuroimage. 2011; 56:1993–2010. [PubMed: 21440071]

Wang L, Beg F, Ratnanather T, Ceritoglu C, Younes L, Morris JC, Csernansky JG, Miller MI. Large deformation diffeomorphism and momentum based hippocampal shape discrimination in dementia of the Alzheimer type. IEEE Trans Med Imaging. 2007; 26:462–470. [PubMed: 17427733]

Wang L, Miller JP, Gado MH, McKeel DW, Rothermich M, Miller MI, Morris JC, Csernansky JG. Abnormalities of hippocampal surface structure in very mild dementia of the Alzheimer type. Neuroimage. 2006; 30:52–60. [PubMed: 16243546]

Wang L, Swank JS, Glick IE, Gado MH, Miller MI, Morris JC, Csernansky JG. Changes in hippocampal volume and shape across time distinguish dementia of the Alzheimer type from healthy aging. Neuroimage. 2003; 20:667–682. [PubMed: 14568443]

West MJ, Kawas CH, Stewart WF, Rudow GL, Troncoso JC. Hippocampal neurons in pre-clinical Alzheimer's disease. Neurobiol Aging. 2004; 25:1205–1212. [PubMed: 15312966]

Whitehouse PJ, Price DL, Struble RG, Clark AW, Coyle JT, Delon MR. Alzheimer's disease and senile dementia: loss of neurons in the basal forebrain. Science. 1982; 215:1237–1239. [PubMed: 7058341]

Woods RP. Characterizing volume and surface deformations in an atlas framework: Theory, applications, and implementation. Neuroimage. 2003; 18:769–788. [PubMed: 12667854]

Younes L, Ratnanather JT, Brown T, Aylward E, Nopoulos P, Johnson H, Magnotta VA, Paulsen JS, Margolis RL, Albin RL, Miller MI, Ross CA. and the PREDICT-HD Investigators and Coordinators of the Huntington Study Group. Regionally selective atrophy of subcortical structures in prodromal HD as revealed by statistical shape analysis. Hum Brain Mapp. 2012 n/a–n/a.

APPENDIX. Manual Delineation Protocol

Hippocampus

The hippocampus is a horseshoe shaped structure with interfolded layers that plays a central role in the limbic system. It is located within the temporal lobe, posterior to the amygdala. The first anterior slice of the hippocampus head appears as a thin stripe right inferior to the amygdala and superior to the entorhinal cortex with its alvear white matter as a well-defined boundary. The superior boundary of the hippocampus is the amygdala while its inferior boundary is the white matter of the temporal lobe that separates it from the entorhinal cortex and the parahippocampal gyrus. Its lateral boundary is the temporal horn of the lateral ventricle and the medial boundary is the well-contrasted cerebral spinal fluid (CSF). Moving posteriorly, the hippocampus gradually replaces the amygdala. It is then surrounded by the white matter of the temporal lobe and the crus of the fornix. The hippocampus disappears when the splenium of the corpus callosum stops connecting the two brain hemispheres.

For segmenting the hippocampus into subregions, due to contrast limit, we decided to divide the hippocampus into three subregions: Cornu Ammonis 1 (CA1), a subregion containing CA2, CA3, and dentate gyrus (CA2+CA3+DG), subiculum (SUB). In coronal slices, the CA1 appears first to be inferior to the amygdala and superior to the SUB. Moving posteriorly, the part CA2+CA3+DG appears to be wrapped around by CA1 and SUB. The CA1 moves laterally and appears as a crescent with the temporal horn of the lateral ventricle as its lateral boundary and the white matter of the temporal lobe as its inferior boundary. The SUB subsequently moves medially as a thin stripe adjacent to the CA1 and lateral to the uncal sulcus. The CA2+CA3+DG part stays inferior to the amygdala and medial to the temporal horn of the lateral ventricle. Its lateral boundary is the CA1 and its inferior boundary is the SUB. In the last few slices, the CA2+CA3+DG part appears to be surrounded by the crus of fornix and the lateral ventricle. The boundaries among the three subregions are also more defined in sagittal view.

Amygdala

The amygdala is a complex structure that is located in the medial temporal lobe, inferior to the putamen and the globus pallidus and anterior to the hippocampus. The first anterior slice of the amygdala appears as an ovoid shape when the temporal lobe already connects to the frontal lobe by a visible limen insulae. The superior boundary of the amygdala is the endorhinal sulcus while its inferior boundary is the white matter that separates it from the parahippocampal gyrus. Its lateral boundary is the white matter of the temporal lobe and its medial boundary is marked distinctively by CSF and the semiannular sulcus. Moving posteriorly, the inferior boundary of the amygdala is the uncal recess of the temporal horn of lateral ventricle and the alvear white matter of the hippocampus. The amygdala subsequently becomes smaller and is replaced by the hippocampus. In caudal slices, the amygdala appears as a thin gray matter stripe superior to hippocampus and inferior to the globus pallidus and then gradually disappears.

In our protocol for the manual delineation of the subregions of the amygdala, it is traced in the coronal view and divided into four nuclei: lateral nucleus, basolateral nucleus, basomedial nucleus, and centromedial nucleus. The lateral nucleus appears first in a characteristic ovoid shape in more anterior slices when the limen insulae already appears to connect the temporal lobe with the frontal lobe. It becomes bigger when moving posteriorly with the lateral and inferior boundaries defined by the white matter of the temporal lobe. Moving 1 mm posteriorly, the basomedial nucleus starts to appear superior to the lateral nucleus with the endorhinal sulcus and the white matter of temporal lobe as superior and medial boundaries. When the semiannular sulcus appears, the basolateral nucleus starts to appear as stripes inferior to the basomedial nucleus and superior to the lateral nucleus. Moving more posteriorly, the hippocampus head appears medially to the basolateral nucleus and the temporal horn of the lateral ventricle becomes the lateral boundary of the lateral nucleus. The centromedial nucleus starts to appear superior to the basomedial nucleus and inferior to the putamen and the globus pallidus. Moving caudally, the hippocampus starts to replace the amygdala and the lateral nucleus, the basolateral nucleus and the basomedial nucleus start to be smaller and then disappear. The temporal horn of the lateral ventricle appears between the hippocampus and the amygdala and becomes the inferior boundary of the centromedial nucleus. The centromedial nucleus appears as a thin gray matter stripe above the hippocampus and gradually disappears.

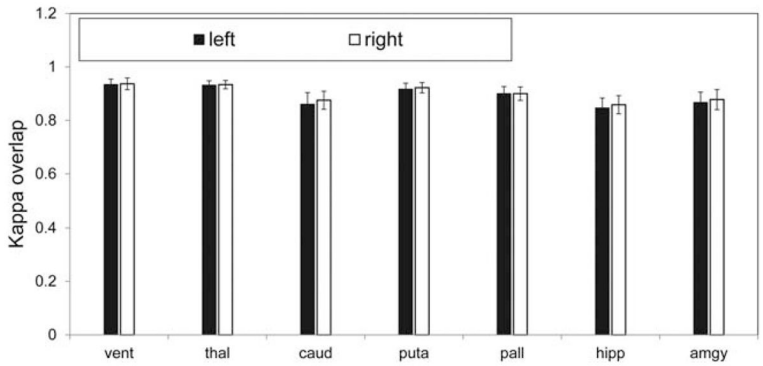

Figure 1.

This figure shows the mean and the standard deviations of the Kappa Overlaps between the segmentations from the denoising pipeline and the original FreeSurfer segmented volumes. Black and white bars respectively denote left and right structures. Vent: lateral ventricles, thal: thalamus, caud: caudate, puta: putamen, pall: pallidum, hipp: hippocampus, amyg: amygdala.

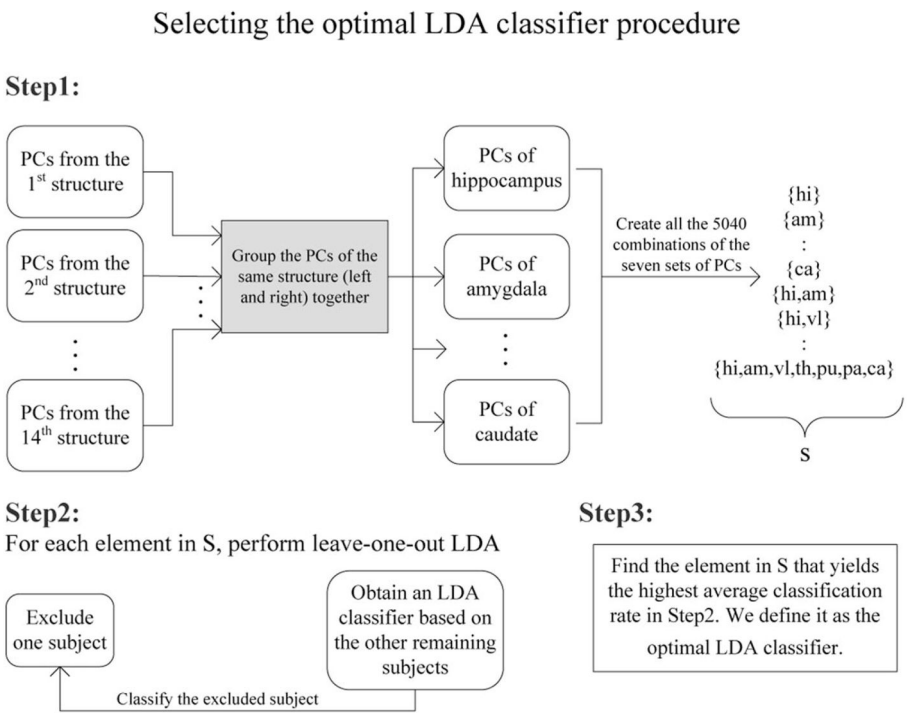

Figure 2.

This figure summarizes the procedure of selecting the optimal LDA classifier based on the PCs from all the fourteen structures, including three steps. Step 1 is to create all the combinations of PCs, resulting in a total of 127. Step 2 is to test the mean classification rate for each set of PCs, based on leave-one-out LDA. Step 3 is to select the LDA classifier with the highest mean correct classification rate in Step 2. Hi: hippocampus, am: amygdala, vl: lateral ventricle, th: thalamus, pu: putamen, pa: pallidum, ca: caudate.

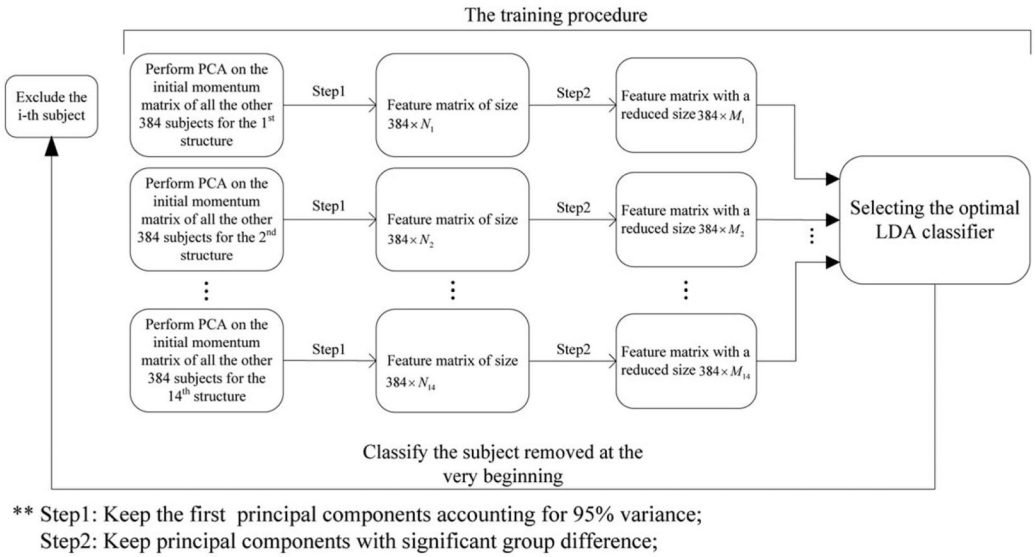

Figure 3.

This figure summarizes the leave-one-out cross-validation procedure of testing the true classification rate that we would be able to yield using our procedure.

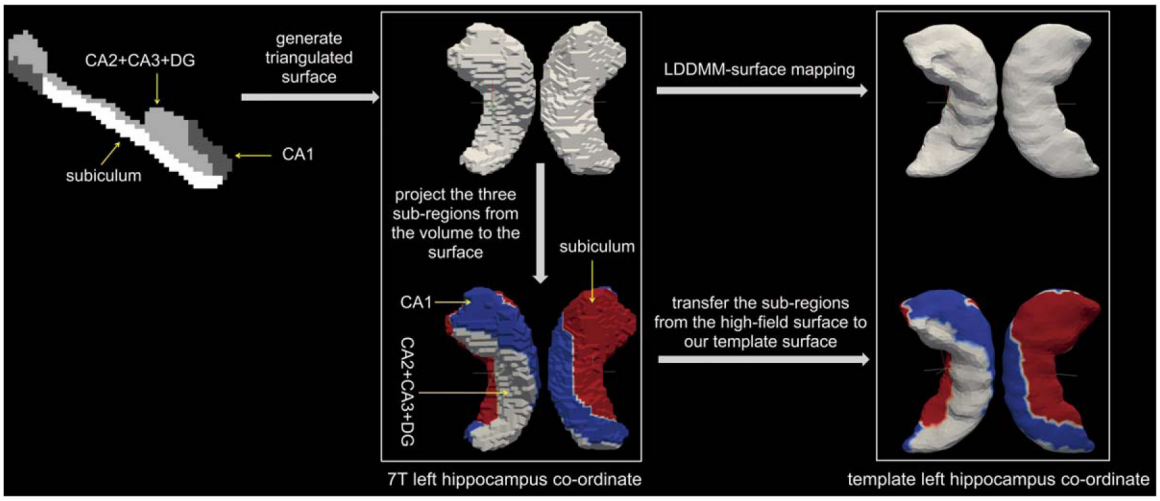

Figure 4.

This figure illustrates the scheme of projecting the three subsegmentations of left hippocampus from a 7.0T high-field MRI image to the template surface, including: manually segmenting the left hippocampus of the 7.0T MR scan into three regions—CA1, CA2+CA3+DG, and subiculum; generating the triangulated surface for the left hippocampus of the 7.0T data; projecting the three subregions of the volume onto the mother hippocampus surface; performing LDDMM-surface mapping between the 7T hippocampus surface and our template surface; transferring the three subregions onto our template left hippocampus surface. [Color figure can be viewed in the online issue, which is available at wileyonlinelibrary.com.]

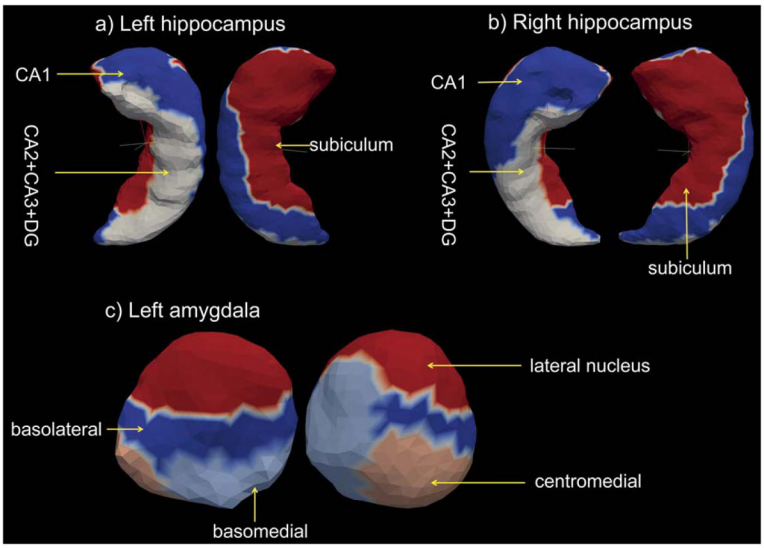

Figure 5.

This figure illustrates the subsegmentations of the left hippocampus (**a**), the right hippocampus (**b**), and the left amygdala (**c**) by projecting the boundaries onto the corresponding mother surface. [Color figure can be viewed in the online issue, which is available at wileyonlinelibrary.com.]

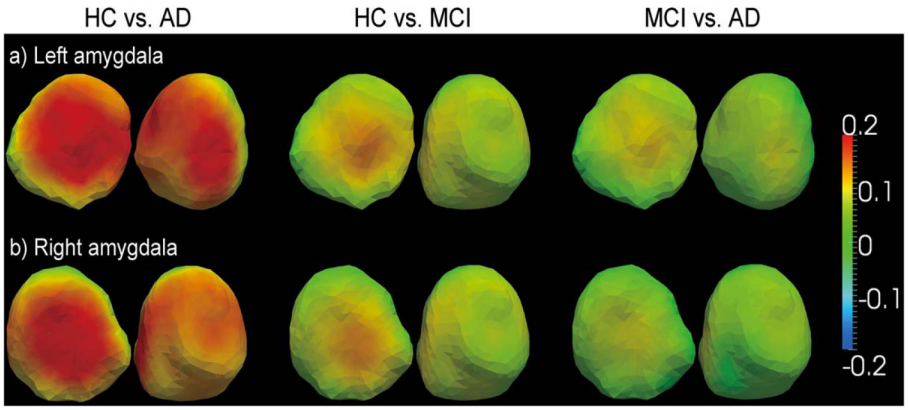

Figure 6.

a) and **b**) respectively show the group shape differences between HC and AD, HC and MCI, as well as MCI and AD measured in left and right amygdala. Both superior (left) and inferior (right) views are displayed for each group comparison. Negative color scale values indicate surface expansion in the latter group, and positive values indicate atrophy. The scale value quantifies the ratio of the local volume of the former group at a particular location to that of the latter group in logarithmic scale. [Color figure can be viewed in the online issue, which is available at wileyonlinelibrary.com.]

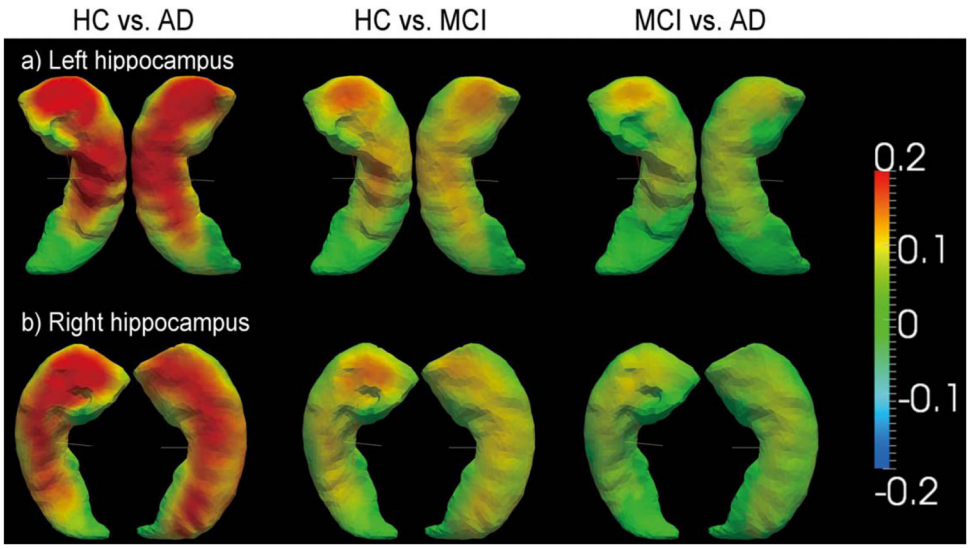

Figure 7.

a) and **b**) demonstrate the group shape differences between HC and AD, HC and MCI, MCI and AD of hippocampus in both hemispheres. Both superior (left) and inferior (right) views are displayed for each group comparison. Negative color scale values indicate surface expansion in the latter group, and positive values indicate atrophy. The scale value measures the ratio of the local volume of the former group to that of the latter group in logarithmic scale. [Color figure can be viewed in the online issue, which is available at wileyonlinelibrary.com.]

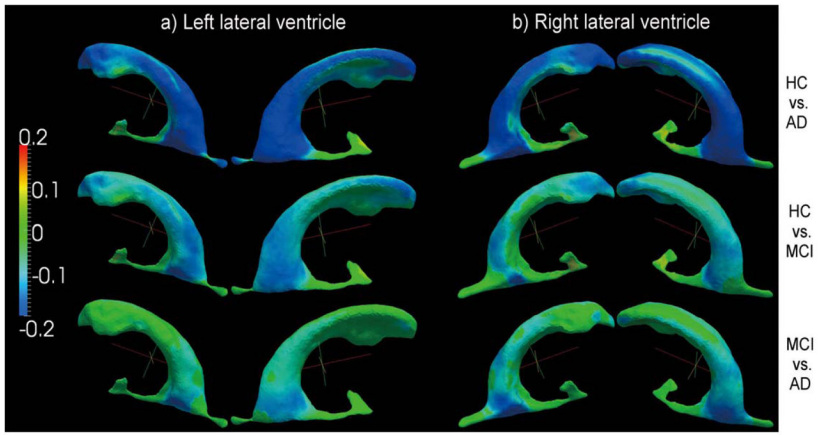

Figure 8.

Group shape differences detected in the lateral ventricles in both hemispheres. Colors corresponding to negative values indicate local expansion of surfaces in the latter group whereas positive values imply atrophy, compared with the former group. The more negative the value, the more prominent the expansion. The scale value measures the ratio of the local volume of the former group to that of the latter group in logarithmic scale. [Color figure can be viewed in the online issue, which is available at wileyonlinelibrary.com.]

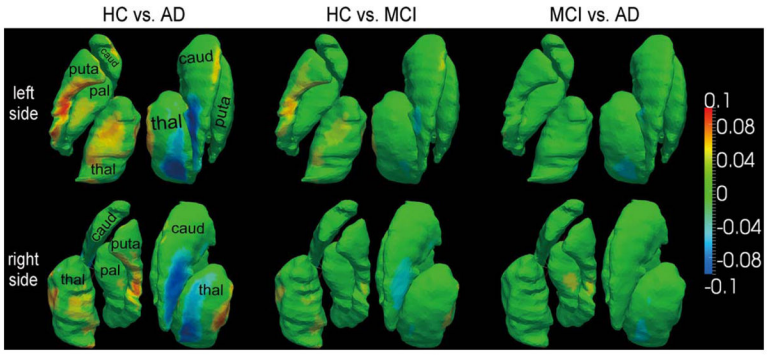

Figure 9.

Surface deformation differences between HC and AD, HC and MCI, as well as MCI and AD in basal ganglia regions and the thalamus. Colors corresponding to negative values indicate local expansion of surfaces in the latter group, compared with the former group, whereas positive indicates atrophy in the latter group. The scale value quantifies the ratio of the local volume of the former group to that of the latter group in logarithmic scale. [Color figure can be viewed in the online issue, which is available at wileyonlinelibrary.com.]

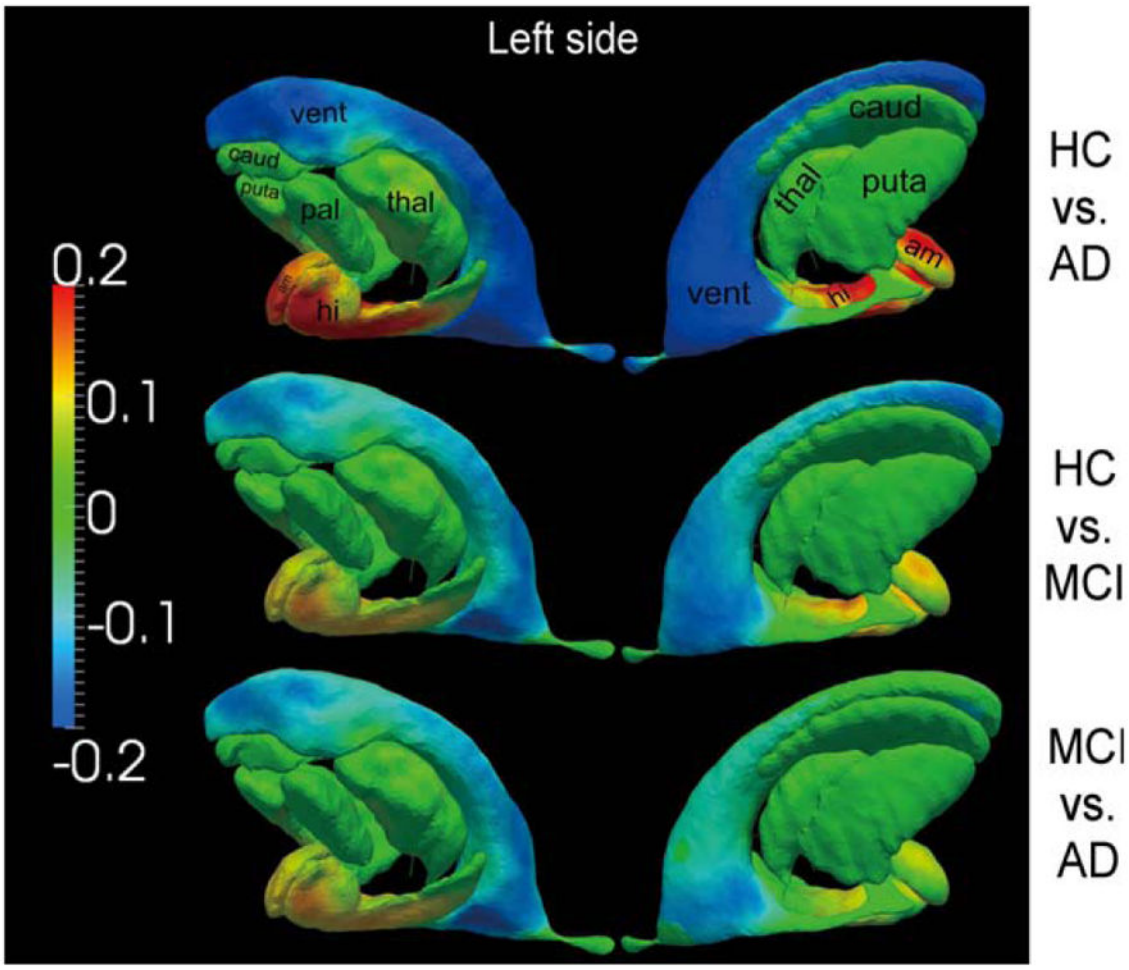

Figure 10.

Group differences, between every two of the three groups, measured in the surfaces of all the seven structures in the left hemisphere. Warm color denotes regions where the corresponding structure has significant atrophy in the latter group when compared with the former group. Cool color suggests local expansion of the structure in the latter group when compared with the former group. Am: amygdala, hi: hippocampus, vent: lateral ventricle, thal: thalamus, puta: putamen, pal: globus pallidus, caud: caudate. The scale value measures the ratio of the local volume around a particular vertex of the former group to that of the latter group in logarithmic scale. [Color figure can be viewed in the online issue, which is available at wileyonlinelibrary.com.]

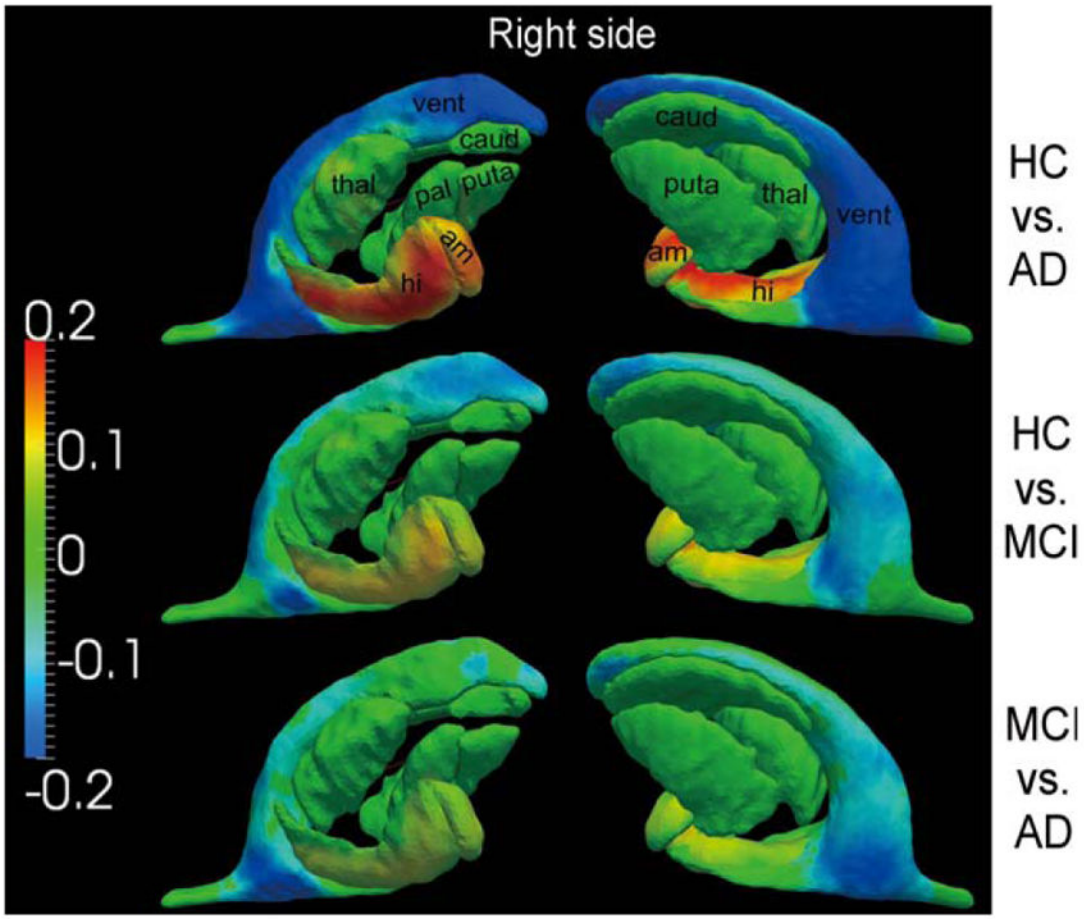

Figure 11.

Group shape variations of all the seven structure in the right hemisphere. Colors corresponding to positive values indicate regions on the structure where there is significant atrophy in the latter group when compared with the former group. Colors corresponding to the negative values suggest local expansion on the structure in the latter group, compared with the former one. Am: amygdala, hi: hippocampus, vent: lateral ventricle, thal: thalamus, puta: putamen, pal: globus pallidus, caud: caudate. The scale value measures the ratio of the local volume of the former group to that of the latter group in the logarithmic scale. [Color figure can be viewed in the online issue, which is available at wileyonlinelibrary.com.]

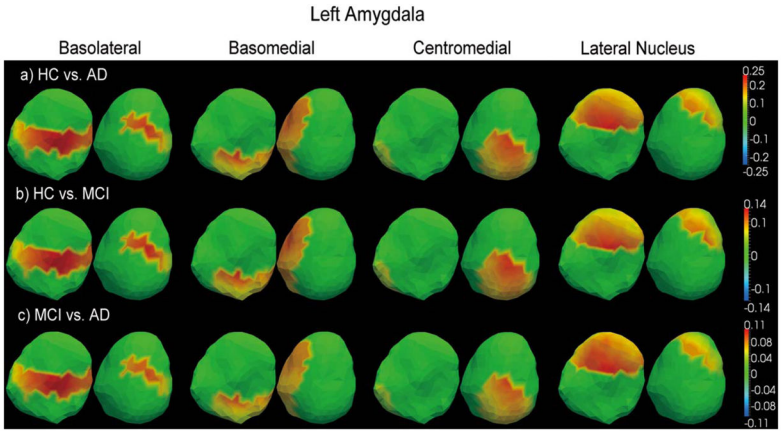

Figure 12.

a)–**c**) respectively show the shape differences between HC and AD, HC and MCI, as well as MCI and AD in the four subregions of left amygdala. Different color scale ranges have been adopted for different comparisons. Warm color indicates regions where atrophy was detected in the latter group as compared with the former group. Cool color indicates local expansion in the region in the latter group when compared with the former group. The scale value measures the ratio of the local volume around each vertex of the template surface measured in the former group to that measured in the latter group in logarithmic scale. [Color figure can be viewed in the online issue, which is available at wileyonlinelibrary.com.]

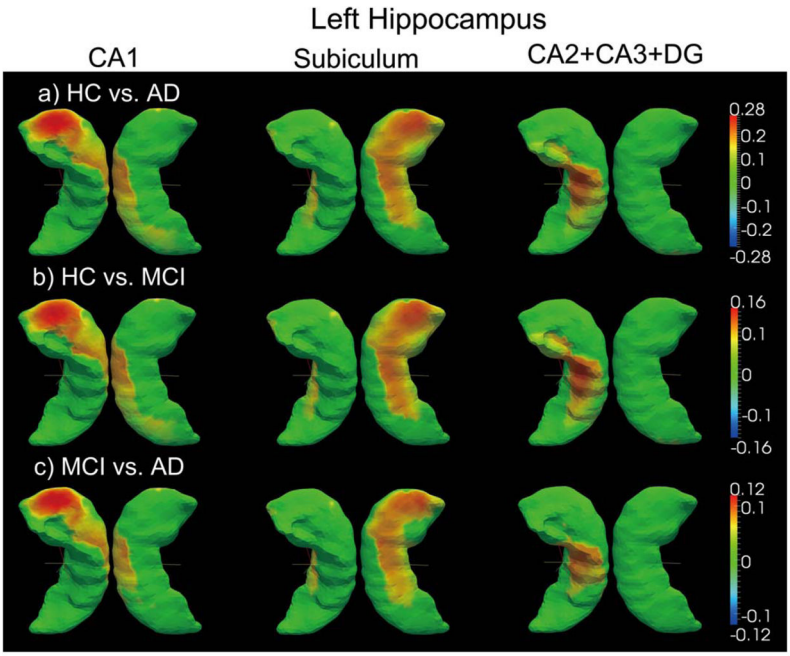

Figure 13.

Group shape differences detected in the three subregions of left hippocampus—CA1, subiculum, and CA2+CA3+DG. Colors corresponding to positive values indicate atrophying regions in the latter group while negative indicates expanding regions in the latter group as compared with the former group. The color scale value quantifies the ratio of the local volume of the former group to that of the latter group in the logarithmic scale. Different color scale ranges have been used for different comparisons. [Color figure can be viewed in the online issue, which is available at wileyonlinelibrary.com.]

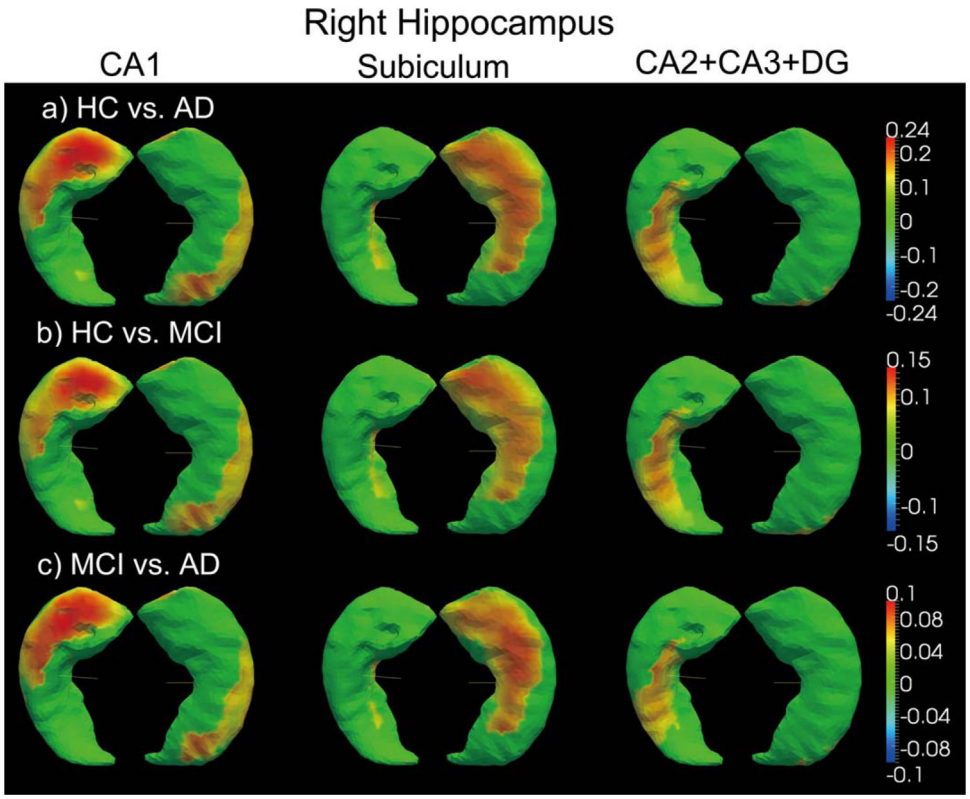

Figure 14.

Group shape differences between HC and AD, HC and MCI, as well as MCI and AD, detected respectively in CA1, subiculum, and CA2+CA3+DG of the right hippocampus. Warm color suggests atrophy while cool color suggests expansion in the latter group when compared with the former group. The scale value measures the ratio of the local volume of the former group to that of the latter group in logarithmic scale. Different color scale ranges have been used for different comparisons. [Color figure can be viewed in the online issue, which is available at wileyonlinelibrary.com.]

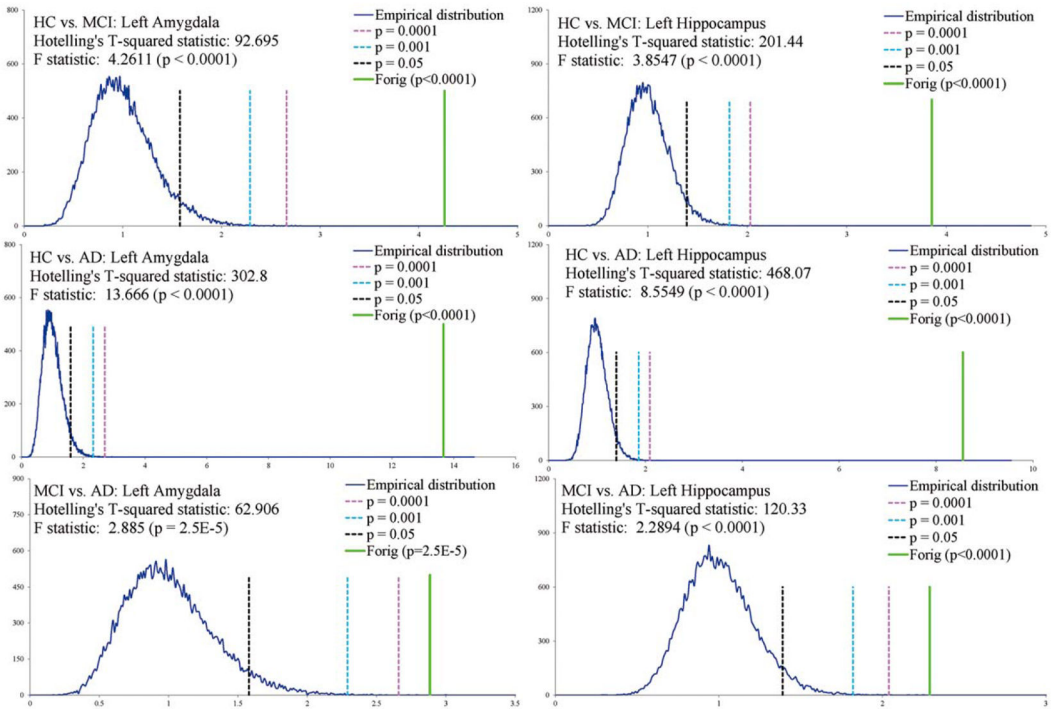

Figure 15.

PCA of the initial momentum matrices of the left hippocampus and the left amygdala. Each subfigure shows the permutation test results for group comparison based on the first *M* PCs that account for 95% of the total variability. Shown are: (1) $F(\hat{T}^2)$ value (solid blue line) of each group comparison (total of three comparisons); (2) $p = 0.0001$ (red dot line), $p = 0.001$ (blue dot line), and $p = 0.05$ (black dot line) for reference; (3) *p*-value derived from the 40,000 permutation tests (solid green line). [Color figure can be viewed in the online issue, which is available at wileyonlinelibrary.com.]

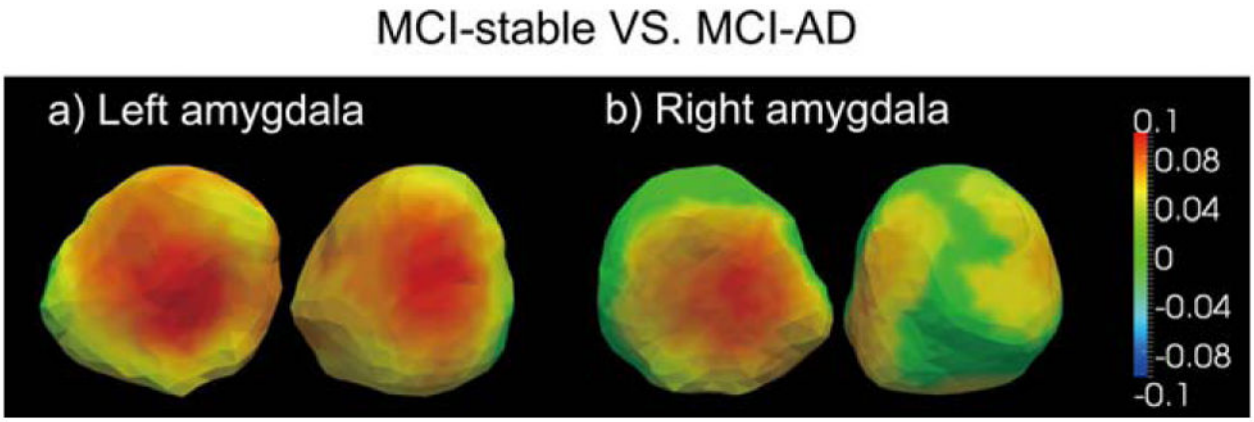

Figure 16.

a) and **b**) display group differences, detected in the left and right amygdala, between the two subtypes MCI-stable and MCI-AD. Positive values indicate atrophy in MCI-AD while negative indicates expansion as compared with MCI-stable. The scale value measures the ratio of the local volume around each vertex on the template surface of the MCI-stable group to that of the MCI-AD in logarithmic scale. [Color figure can be viewed in the online issue, which is available at wileyonlinelibrary.com.]

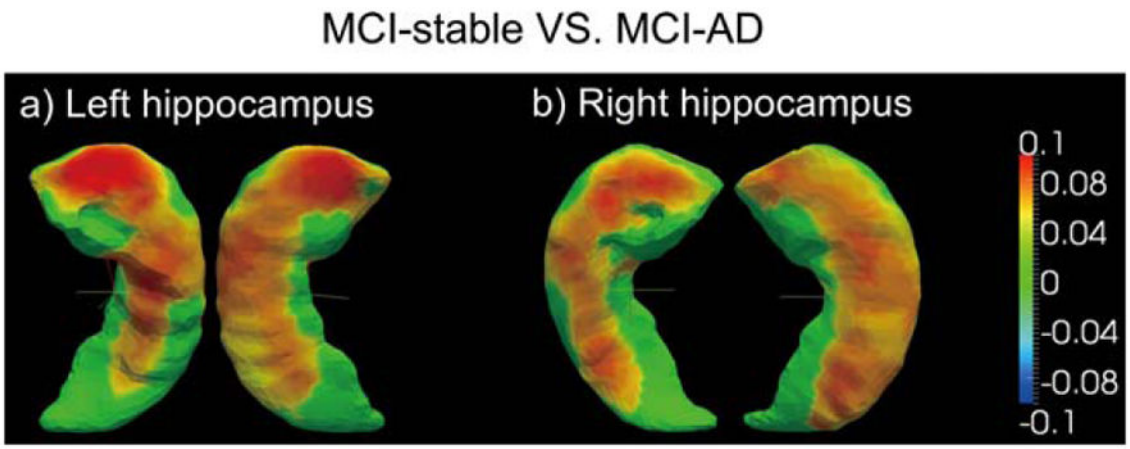

Figure 17.

Hippocampal shape differences between MCI-stable and MCI-AD. Warm color indicates regions on the hippocampus where significant atrophy has been detected in MCI-AD when compared with MCI-stable, whereas cool color indicates expansion. The scale value measures the ratio of the local volume of the hippocampus in MCI-stable to that in MCI-AD in the logarithmic scale. [Color figure can be viewed in the online issue, which is available at wileyonlinelibrary.com.]

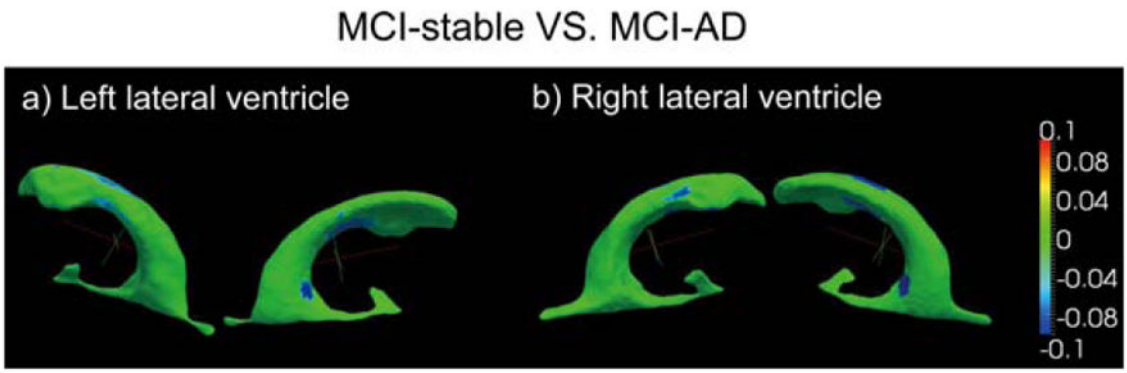

Figure 18.

Shape differences between MCI-stable and MCI-AD detected on lateral ventricles in both hemispheres. The color corresponding to value 0 suggests no regional shape variation. Colors corresponding to negative values suggest expanding regions in MCI-AD when compared with MCI-stable, while those corresponding to positive values indicate atrophy in MCI-AD. The scale value measures the ratio of the local volume of the lateral ventricle in MCI-stable to that in MCI-AD in logarithmic scale. [Color figure can be viewed in the online issue, which is available at wileyonlinelibrary.com.]

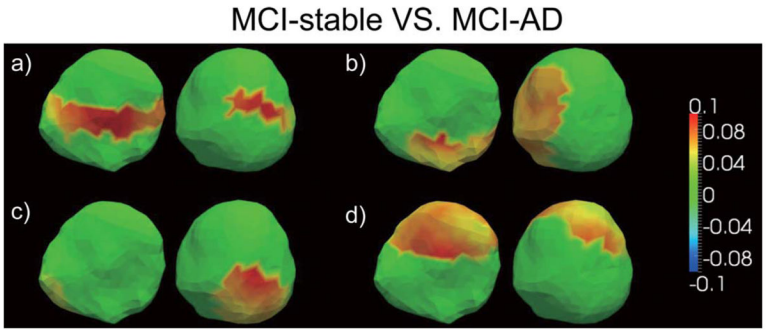

Figure 19.

Shape difference between MCI-stable and MCI-AD in terms of the four subregions of left amygdala – basolateral (panel (a)), basomedial (panel (b)), centromedial (panel (c)), and lateral nucleus (panel (d)). Warm color suggests atrophying regions in MCI-AD while cool color suggests expanding regions when compared with MCI-stable. The scale value measures the ratio of the local volume of each subregion in MCI-stable to the local volume in MCI-AD in logarithmic scale. [Color figure can be viewed in the online issue, which is available at wileyonlinelibrary.com.]

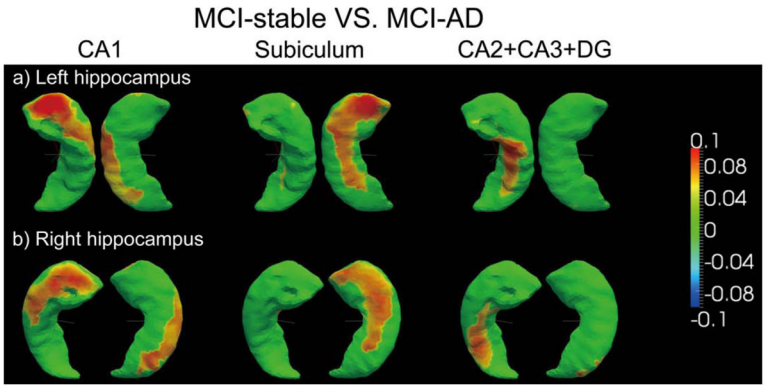

Figure 20.

Shape differences between MCI-stable and MCI-AD detected on the three subregions of the hippocampus. Positive values indicate atrophying regions in MCI-AD while negative values indicate expanding regions as compared with MCI-stable. The scale value measures the ratio of the local volume of the former group to that of the latter group in logarithmic scale. [Color figure can be viewed in the online issue, which is available at wileyonlinelibrary.com.]

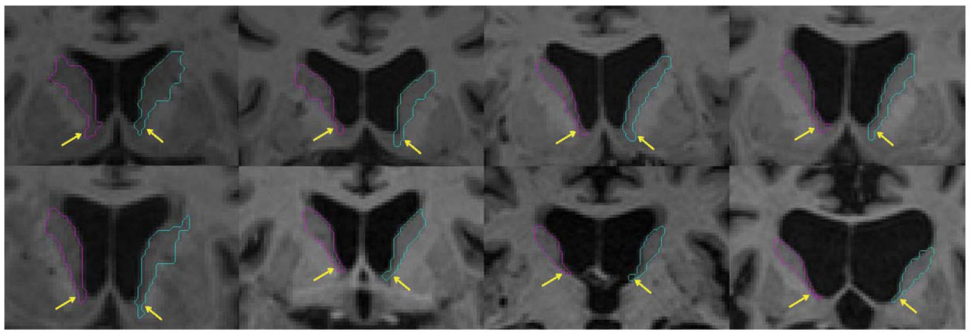

Figure 21.

Automated volume segmentations of caudate from FreeSurfer for representative subjects. [Color figure can be viewed in the online issue, which is available at wileyonlinelibrary.com.]

TABLE I

Demographic data

Parameter	HC Group (*n* =210)	MCI Group (*n* =369)	AD Group (*n* =175)
Subject age (yr)	76.25 ±5.01	75.03 ±7.32	75.28 ±7.49
No. male subjects	109	236	94
MMSE score	29.12 ±1.02	27.01 ±1.76	23.43 ±2.01
CDR-SB score	0.03 ±0.12	1.60 ±0.89	4.23 ±1.64

TABLE II

Average volume measurements (mm^3) of the original segmentations from Freesurfer and those "filtered" from the LDDMM-based pipeline as well as their mean differences

	Original segmentation	Filtered segmentation	Mean volume difference (%)
lvent	22,132	21,899	1.05
lthal	6,395	6,255	2.18
lcaud	3,362	2,981	11.34
lputa	4,648	4,456	4.14
lpall	1,631	1,517	6.98
lhipp	3,165	2,971	6.12
lamyg	1,299	1,212	6.72
rvent	20,360	20,887	2.56
rthal	6,214	6,033	2.92
rcaud	3,454	2,964	14.21
rputa	4,608	4,453	3.37
rpall	1,655	1,513	8.61
rhipp	3,312	3,093	6.60
ramyg	1,318	1,228	6.88

lvent: left lateral ventricle, ltha: left thalamus, lcaud: left caudate, lputa: left putamen, lpall: left globus pallidus, lhipp: left hippocampus, lamyg: left amygdala, rvent: right lateral ventricle, rtha: right thalamus, rcaud: right caudate, rputa: right putamen, rpall: right globus pallidus, rhipp: right hippocampus, ramyg: right amygdala.

TABLE III

A comparison of the upper bounds of the confidence intervals for *p*-values obtained from the volume analysis and the PCA-based shape analysis for each structure

	HC vs. AD		HC vs. MCI		MCI vs. AD	
	Volume analysis	**Shape analysis**	**Volume analysis**	**Shape analysis**	**Volume analysis**	**Shape analysis**
lamyg	$p < 1 E -4$	$p < 1 E -4$	$p < 1 E -4$	$p < 1.4 E -4$	$p < 1 E -4$	$p < 1 E -4$
ramyg	$p < 1 E -4$	$p < 1 E -4$	$p < 1 E -4$	$p < 1 E -4$	$p < 1 E -4$	$p < 1 E -4$
lhipp	$p < 1 E -4$	$p < 1 E -4$	$p < 1 E -4$	$p < 1 E -4$	$p < 1 E -4$	$p < 1 E -4$
rhipp	$p < 1 E -4$	$p < 1 E -4$	$p < 1 E -4$	$p < 2.6 E -4$	$p < 1 E -4$	$p < 1 E -4$
lvent	$p < 1 E -4$	$p < 1 E -4$	$p < 0.04$	$p < 1 E -4$	$p < 1 E -4$	$p < 1 E -4$
rvent	$p < 1 E -4$	$p < 1 E -4$	$p < 5 E -3$	$p < 3.7 E -4$	$p < 1 E -4$	$p < 1 E -4$
lcaud	$p < 0.46$	$p < 1 E -4$	$p < 0.52$	$p < 0.07$	$p < 0.15$	$p < 3.7 E -4$
rcaud	$p < 0.89$	$p < 1 E -4$	$p < 0.19$	$p < 0.01$	$p < 0.17$	$p < 0.12$
lputa	$p < 0.02$	$p < 1 E -4$	$p < 0.47$	$p < 1 E -4$	$p < 0.05$	$p < 5.9 E -4$
rputa	$p < 0.04$	$p < 1 E -4$	$p < 0.95$	$p < 2.6 E -4$	$p < 0.02$	$p < 5.6 E -3$
lthal	$p < 0.07$	$p < 1 E -4$	$p < 0.96$	$p < 1.2 E -4$	$p < 0.09$	$p < 4 E -4$
rthal	$p < 0.05$	$p < 1 E -4$	$p < 0.67$	$p < 1 E -4$	$p < 0.1$	$P < 1 E -3$
lpall	$p < 0.08$	$p < 1 E -4$	$p < 0.27$	$p < 0.21$	$p < 5 E -3$	$p < 1.3 E -3$
rpall	$p < 0.45$	$p < 1 E -4$	$p < 0.12$	$p < 2 E -3$	$p < 0.02$	$p < 0.02$

vent: left lateral ventricle, ltha: left thalamus, lcaud: left caudate, lputa: left putamen, lpall: left globus pallidus, lhipp: left hippocampus, lamyg: left amygdala, rvent: right lateral ventricle, rtha: right thalamus, rcaud: right caudate, rputa: right putamen, rpall: right globus pallidus, rhipp: right hippocampus, ramyg: right amygdala

TABLE IV

A comparison of the specificity and the sensitivity obtained from the LDA classifiers built respectively from the volume information and the shape information for each structure

	Specificity		Sensitivity	
	Volume information (%)	**Shape information (%)**	**Volume information (%)**	**Shape information (%)**
Amyg	75	80	72	78
Hipp	76	86	74	81
Vent	73	83	53	79
Caud	47	68	58	68
Puta	53	75	58	78
Thal	49	76	58	75
Pall	51	68	54	68